47th AIAA/ASME/SAE/ASEE Joint Propulsion Conference & Exhibit
31 July - 03 August 2011, San Diego, California

AIAA 2011-6065

Sounding Rocket Energy Management Using Cold-Gas Aerospike Thrusters

Stephen A. Whitmore[1] and Andrew R. Bath[2]
Utah State University, Logan, UT, 84322-4130

And

The Undergraduates of the Chimaera MAE 4800 Senior Design Team

The design of a cold-gas energy management system for an amateur-class sounding rocket is presented. The design is an outcome of a required one-year senior design capstone course taught by the Mechanical and Aerospace Engineering Department at Utah State University. This course targets NASA's University Student Launch Initiative (USLI) competition organized and directed by Marshall Spaceflight Center. The design features a solid propellant primary rocket motor that provides a majority of launch impulse, and a secondary propulsion system that manages the energy level of the vehicle to reach a target apogee altitude. The secondary propulsion system was flown as the "engineering payload" for the USLI competition. The secondary system features a pulse-modulated cold gas bleed system with expansion ramps designed from aerospike nozzle theory. The energy management system was integrated with the airframe by placing the aerospike ramps around the primary solid motor case; this design added minimal aerodynamic drag to the configuration. Onboard navigation data are processed in a small onboard avionics computer to continuously estimate the total specific energy and potential altitude of the vehicle. When, required the onboard avionics activate the system to boost the energy level of the vehicle. Ground and flight test results are presented.

Nomenclature

A	=	state equation dynamics matrix
A_{ref}	=	vehicle reference area based on maximum diameter, cm^2
A_x	=	longitudinal acceleration, *g's*
A_y	=	lateral acceleration, *g's*
A_z	=	normal acceleration, *g's*
B	=	state equation input matrix
C	=	measurement equation matrix
C_D	=	drag coefficient
C_{D0}	=	incompressible drag coefficient
C_g	=	longitudinal center of gravity, *cm*
C_L	=	lift coefficient
C_m	=	pitching moment coefficient
c_p	=	aerospike ramp pressure coefficient
C_p	=	longitudinal aerodynamic center of center of pressure, *cm*
D_{body}	=	body tube diameter, *cm*
E	=	total energy of the vehicle, *joules*
g	=	local acceleration of gravity, m/sec^2
g_0	=	standard acceleration of gravity, 9.8067 m/sec^2
h	=	altitude, *m*
h_{apogee}	=	apogee altitude, *m*
h_{min}	=	minimum altitude for energy augmentation, *m*

[1] Associate Professor, Mechanical and Aerospace Engineering Department, 4130 Old Main Hill/UMC 4130, Associate Fellow, AIAA.
[2] Graduate research Assistant, Mechanical and Aerospace Engineering Department, 4130 Old Main Hill/UMC 4130, Student Member, AIAA.

$h_{perfectflite}$	=	PerfectFlite® altitude measurement, *m*
$h_{potential}$	=	potential altitude, *m*
h_{target}	=	target altitude, *1609.32 m*
I	=	identity matrix
I_{sp}	=	specific impulse, *s*
k	=	discrete time index
K	=	Kalman gain matrix
m	=	vehicle mass, *k*
$M_{\{ij\}}$	=	component of direction cosine matrix
M_∞	=	free stream Mach number
p	=	roll rate or static pressure, *deg/sec* or *kPa*
p_∞	=	free stream pressure, *kPa*
P_c	=	plenum or chamber pressure, *kPa*
$P_{(ij)}$	=	Kalman Filter state estimate covariance matrix
P_0	=	stagnation pressure, *kPa*
q	=	pitch rate, *deg/sec*
Q	=	state noise covariance matrix
r	=	yaw rate or radial position, *deg/sec* or *cm*
R	=	measurement noise variance, m^2
t	=	time, *s*
t_{apogee}	=	time to apogee, *s*
u	=	body-axis longitudinal velocity, *m/sec*
U	=	state equation input vector
u/V	=	normalized velocity defect
v	=	body axis lateral velocity, *m/sec*
V	=	velocity, *m/sec*
$V_{horizontal}$	=	horizontal velocity, *m/sec*
w	=	body axis normal velocity, *m/sec*
x_{cg}	=	longitudinal center of gravity, *cm*
x_{cp}	=	longitudinal center of pressure, *cm*
y	=	lateral position behind model, *cm*
z	=	vertical position behind model, *cm*
α	=	angle of attack, *deg*
χ	=	static margin
δ_{wake}	=	wake width, *cm*
$\Delta h_{potential}$	=	available change in potential altitude, *m*
ΔV	=	available change in velocity, *m/sec*
Δt	=	sample interval, *sec*
ε	=	measurement noise weighting function safety factor
γ	=	flight path angle, *deg.*
ϕ	=	roll angle, *deg*
Φ	=	state transition matrix
ρ	=	density, kg/m^3
σ^2	=	variance of a parameter or noise covariance component
ψ	=	yaw angle, *deg*
τ	=	Kalman Filter time constant, *sec*
θ	=	pitch angle, *deg*
ζ	=	circumferential coordinate, *deg.*
$()_k$	=	value at time index *k*
$()_{k/k}$	=	Kalman filter calculation based on *k* measurements
$()_{k+1}$	=	value at time index *k+1*
$()_{k+1/k}$	=	Kalman filter calculation based on *k* measurements
$()_{k+1/k}$	=	Kalman filter calculation vector based on *k* +1 measurements

I. Introduction

THE outcome of a two-semester capstone senior design course developed and implemented by the Mechanical and Aerospace Engineering Department (MAE) at Utah State University (USU) is described herein. This paper is offered as a case study of a successful capstone class that achieved all of its educational and technical objectives, and was selected as the winner of the 2011 NASA University Student Launch Initiative (USLI) competition. It is hoped that the materials presented in this paper will serve as a guide for other academic institutions wishing to undertake a similarly ambitious project. This project clearly demonstrates that when challenged and properly guided, undergraduate students can accomplish amazing things. This design course was unique in that it specifically targeted the USLI launch competition organized and directed by the Marshall Spaceflight Center in Huntsville AL. The USLI competition tasks student teams to design and build a reusable rocket that can carry and safely recover working science or engineering payloads. The USLI competition judges the overall winners according to a scoring rubric that includes design reports and presentations, and a final written report describing the flight experiment results. A key element of the scoring rubric is the "altitude prize" for the team that comes closest to exactly 1-mile above the local ground level (AGL). The USLI concludes each spring with a daylong launch event near NASA's Marshall Space Flight Center. The NASA Office of Education, the Exploration Systems Mission Directorate (ESMD), and the NASA Space Grant Consortium in part sponsored this project. The course materials adhere to the standards of the Accreditation Board for Engineering and Technology (ABET), and are constructed to be relevant to key research areas identified by ESMD.

II. Design Course Overview

As described in the introductory section, the course material developed for this capstone class adheres to ABET-prescribed standards. ABET is recognized by the U.S. Government as the accreditation organization for higher-education programs in applied sciences, engineering, and technology. In the year 2000 ABET established a new program for accreditation review termed Engineering Criteria 2000" (EC2000), EC2000 changed the review perspective from qualitative evaluation to one based on program-defined missions, outcomes, and objectives. A major EC2000 requirement specifically states *"Students must be prepared for engineering practice through a curriculum culminating in a major design experience based on the knowledge and skills acquired in earlier course work and incorporating appropriate engineering standards and multiple realistic constraints."* As defined by ABET "*Engineering design is the multi-disciplinary process of devising a system, component, or process to meet desired needs. It is a decision-making process (often iterative), in which the basic sciences, mathematics, and the engineering sciences are applied to convert resources optimally to meet these stated needs.*" Here students are expected to engage in a culminating major design experience that requires cross-disciplinary efforts and a physical design realization.

Senior design capstone courses, when properly structured, provide students with a unique experience not generally available in an academic environment. Capstone courses involving multiple students require teamwork and application of industry-developed systems engineering processes that span the development cycle of the project. Students must make self-directed decisions to meet program objectives. Making these decisions properly requires significant use of problem solving, measurement, and experimental skills. Selecting a design concept that allows a small-scale prototype-demonstrator to be constructed within the academic-year time and budget constraints is a major challenge. A balance between "achievability" and "creativity" must be struck to achieve a realizable, successful design.

A. The USLI Competition as a Senior Design Capstone Experience

In industry, the client or customer provides much of the program structure including design requirements, budget, and program schedule. These constraints do not exist in an academic design class. Here the instructor must artificially prescribe the budget, design requirements, and schedule; and it is often difficult to get a high level of student interest in these artificially drafted requirements. With an excessively open-ended senior design course, students must be responsible for inventing client requirements, the design methodology, and then eventually constructing a design to meet their own requirements. This is an approach fraught with danger.

One of the major enemies of a successful program is "mission creep." Mission creep more often than not leads to a program stalling or collapsing under its own weight. Because of limited resources and student experience levels, undergraduate design projects are especially susceptible to mission creep. A "tried and true" way to keep a program on track is consistent adherence to a well-defined Design Reference Mission (DRM). A well-defined DRM allows top-level program requirements to be achieved, but limits the design scope and restricts unnecessary requirement growth. Targeting the USLI competition automatically produces a clearly defined DRM.

The USLI competition rules and scoring rubric items are used to set the top-level design requirements for the USU capstone design class. Thus the USLI becomes a natural customer for the class; and getting student "buy-in" is significantly easier. The top-level design schedule and milestones are pre-determined by the USLI competition rules. Students are required to develop and strictly adhere to a project schedule that conforms with the prescribed USLI schedule. The primary project objectives are very clear; fly safely and win the competition! Figure 1 shows the milestone map developed by the design class to successfully navigate all USLI objectives within the NASA mandated competition schedule. The USU Entry into the Competition, officially named "Team Chimaera," was named after a mythical beast that was hybrid of many animal parts. This moniker certainly describes the final design that resulted.

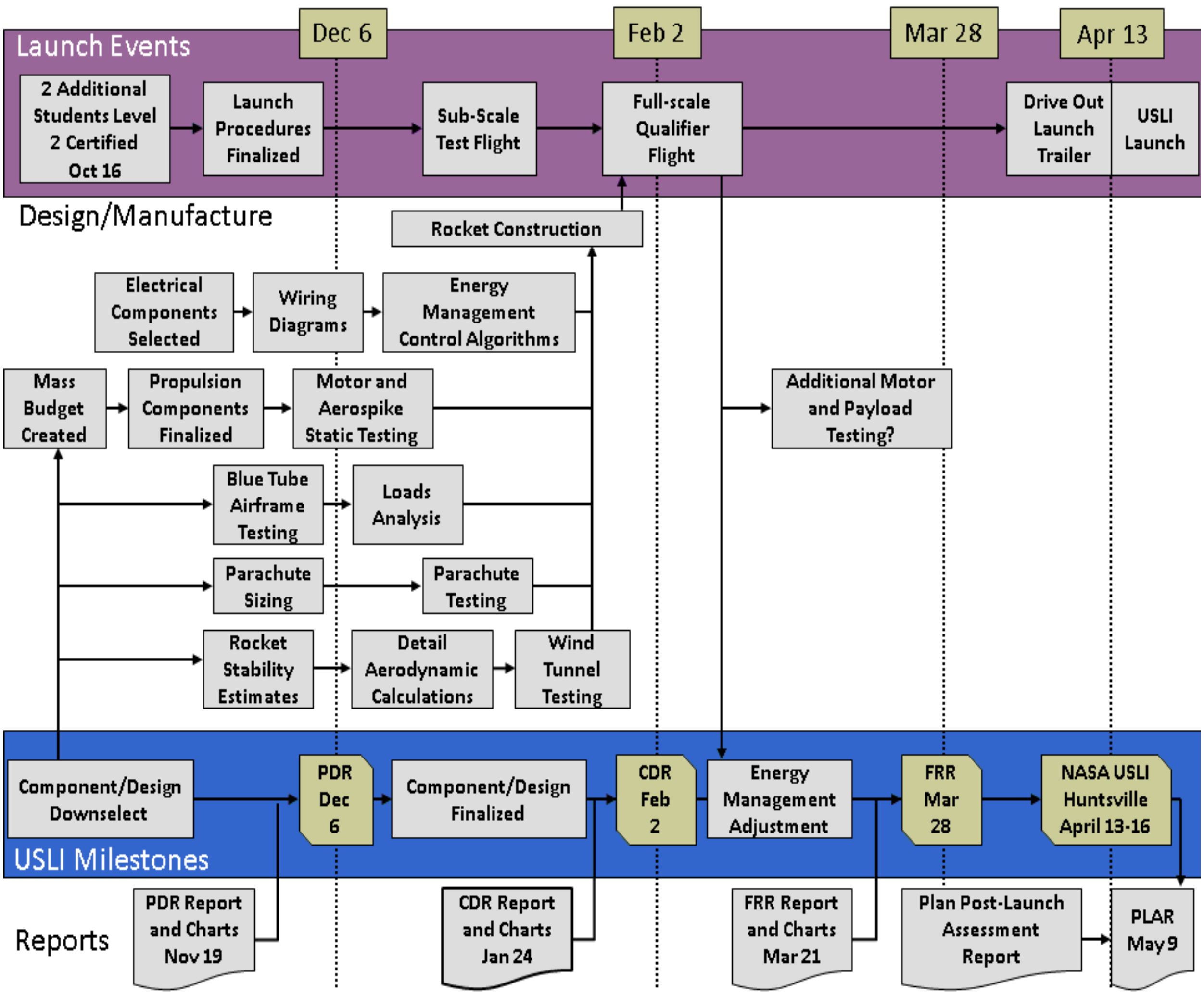

Figure 1. USLI Capstone Design Project Milestone Map.

III. Systems Engineering

The large size of the Chimaera team and the complex interdisciplinary nature of the design project required the use of formal systems engineering and management concepts throughout the class. As feasible these processes were modeled on well-documented, formal processes widely used within NASA, the Department of Defense (DoD), and the aerospace industry. Taking into account that seniors in college lack professional experience and background; as necessary, condensed subject matter lectures were incorporated into the class content. A few of the adapted systems engineering tools and procedures used in the design process will be discussed in eh following sub-sections.

A. Chimaera Design Team Organization

The USLI-prescribed process closely emulates an industry-style design cycle. The USLI competition requires the students to submit a formal response to a NASA-issued Request for Proposal (RFP). The quality of the student team's response to the RFP determines whether or the team is for selected the USLI competition. Once selected, the team must submit to formal design reviews including a preliminary design review (PDR), a critical design review (CDR), and a flight readiness review (FRR). Both written and oral presentations are required. These reviews are major components of the overall USLI scoring rubric.

One of the most important aspects of a capstone design course is the presentation of condensed introductory materials that provide sufficient project background and technical information. This upfront material allows the students to begin making meaningful design contributions very early in the academic year. This early portion of the class also provides assessment metrics that allow students to be assigned to project aspects best suited to their skills and interests. This early evaluation period allows the discipline sub-teams to be optimally populated.

Discipline sub-teams were structured along traditional industry-style management lines. The team elected two undergraduate student members to serve as Chief Engineer and Systems Engineer. Figure 2 shows the project breakdown structure (PBS). The Chimaera team consisted of 13 undergraduate students taking the class for credit and 4 graduate research/teaching assistants. When the faculty instructor was not available, graduate assistants assisted the undergraduate students in various technical discipline areas. The experiences and subject matter expertise provided by graduate assistants were essential to accomplishing the project goals and objectives.

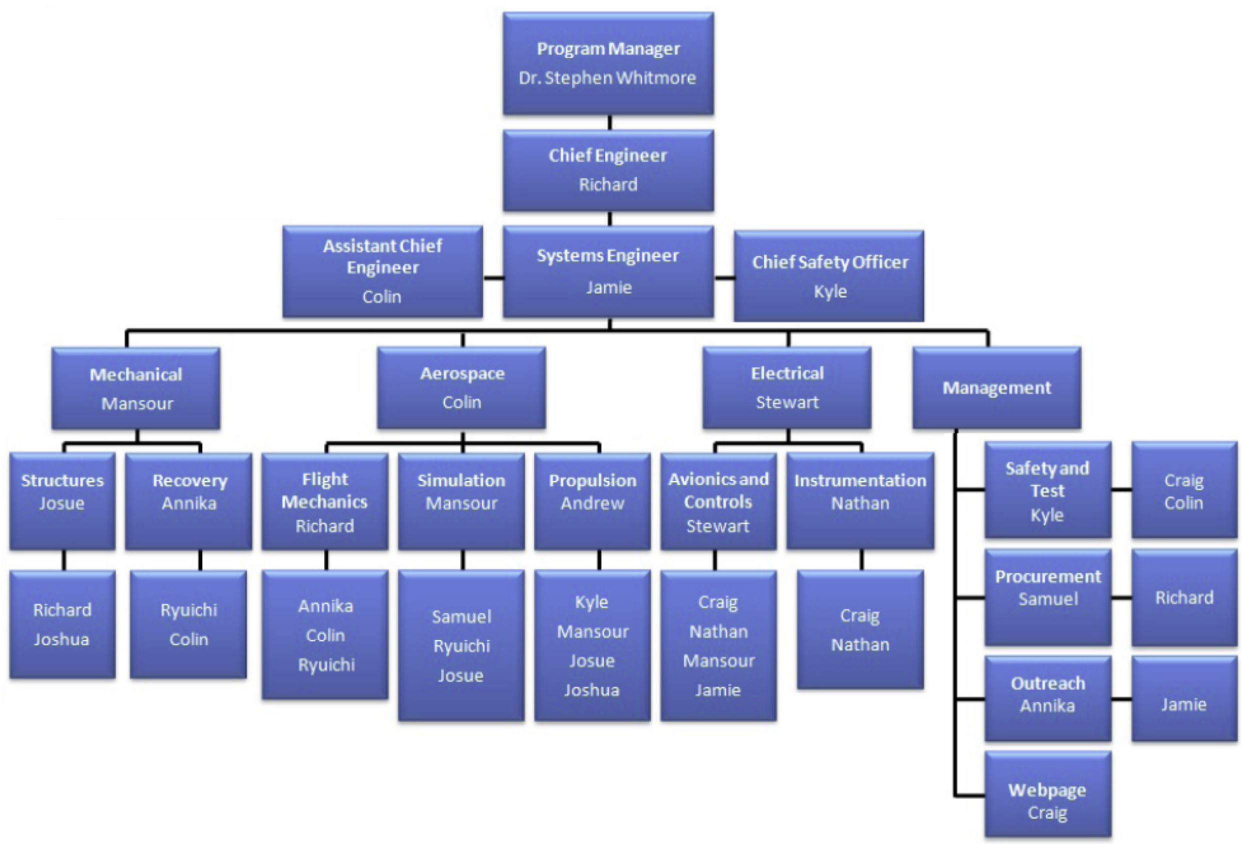

Figure 2. Chimaera Team Project Breakdown Structure (PBS).

B. Requirements Analysis

Top-level design requirements are shown in Table 1. Vehicle design requirements come from three primary sources; 1) USLI competition-specified requirements, 2) compliance with safety codes, and 3) derived-secondary design requirements. The National Association of Rocketry (NAR)[1], and the National Fire Prevention Association (NFPA)[2] specify the primary safety codes governing the rocket operation. Table 1 lists the key requirements followed by the source. In the second column of this table the symbol USLI represents NASA competition rules, NAR and NFPA represent safety code driven requirements, and USU represents secondary, project-derived requirements.

Table 1. Top-Level Design Requirements

Summary of Key Requirements	Source
Rocket shall not fly higher than 5600 feet AGL	USLI
Rocket shall carry scientific payload	USLI
Rocket shall be recoverable and reusable	USLI
Rocket shall land within 2500 ft. of pad	USLI
Cost of flight hardware and payload shall not exceed \$5000	USLI
Students shall do all critical design and fabrication	USLI
Team shall use launch and safety checklists	USLI
Propulsion Requirements • Shall use commercially available certified motor • Total cold-gas impulse less than 320 N-s • Cold gas thrust less than 80 s – NFPA 1122 Code for Model Rocketry – NFPA 1127 Code for High Powered Rocketry	USLI, NAR NFPA NFPA
The rocket shall get within meters of the one mile target altitude • 95% confidence level to resolution of primary sensor • Shall not exceed one mile	USU
The cold gas CO_2 components shall fit within the rocket case (drag minimization)	USU
The rocket shall launch from a rail with velocity no less than 15 m/s	USU
The structural members shall have a 2.5 factor of safety	USU
Shall gather first time in-flight 2D aerospike surface pressure data	USU

B. Review Item Dispensation

A key systems engineering feature was the development of a Review Item Disposition (RID) procedure to ensure fluid communication between sub-teams as well as provide a means of formal documentation for actions performed. This process is modeled on the formal processes widely used within NASA, the Department of Defense (DoD), and the aerospace industry. All RIDs are tracked on a student-built website. This website also presents formal documents such as trade studies, presentations, and test reports. In addition to keeping formal documents on the website, an online "wiki" was developed for easy uploads of information. The "wiki" provided a quick reference for other team members. This wiki archives general knowledge gained this year for future teams. A document control system, using primarily Google Docs™, was created to track the variety of documents created during this project. The website was mandated by USLI competition rules, and its overall quality was scored as a part of the USLI competition rubric.

C. Hazard Analysis

Unlike a simple paper study, this project involved high-powered rocketry, low-grade pyrotechnics, and DOT 1.4[3] ordnance. There exists a real potential for accidents that could cause significant property damage and personnel injury. The Risk Management Office (RMO) at Utah State University was involved in much of the decision-making process for this project, and drove several of the initial decisions that affected the overall system design. To satisfy RMO mandated hazard-reporting requirements, a formal system of risk assessment and mitigation was developed and applied. Figure 3 presents the hazard assessment matrix used for this project. Table 2 describes the likelihood classifications and Table 3 describes the hazard severity classifications. To navigate this matrix, select a risk and determine its likelihood of occurrence, and then assess consequences. For example, the *Hazard Likelihood* for a team member receiving a paper cut during project is fairly high, but the *Magnitude of Failure* is negligible. Therefore, a paper cut is listed as a level-6 hazard. Level 6 is considered to be an acceptably low level of risk and can be "carried" without formal mitigation processes. On the other hand, *Hazard Likelihood* of the rocket becoming unstable during launch is "unlikely," but the *Magnitude of Failure* is "catastrophic." This hazard corresponds to a level 16, or extreme, hazard. Extreme hazards (level 13 and above) are unacceptable and require additional mitigations. In this case mandated significant effort was directed towards managing the vehicle center of gravity, and accurately placing the center of pressure to insure static stability. Multiple analytical calculations and wind tunnel tests were performed to verify vehicle stability,. This assessment matrix was applied to every identified risk to determine if the level of risk is acceptable. If the risk was deemed unacceptable, then the design was modified or processes were developed to mitigate the hazard.

Table 2. Hazard Likelihood Classification

Level	*Likelihood*	*Description*
A	Very Likely	It is likely this event will happen >90% of the time
B	High	This event happens more often than not, 60%
C	Moderate	There is a chance this event will happen, 25%
D	Low	This event rarely happens,1%
E	Very Low	This event occurs less than 0.1%

Table 3. Hazard Severity Classification.

Level	*Severity*	*Description*
I	Catastrophic	**Personnel:** Life threatening or permanent disability **Environment:** Massive, irreparable loss or damage; damage results in legal action **Payload:** Complete system failure without ability to resolve; results in mission failure
II	Extreme	**Personnel:** Injury requiring hospitalization/emergency medical attention **Environment:** Large scale damage **Payload:** System failure
III	Moderate	**Personnel:** Requires medical aid, but manageable with a first-aid kit **Environment:** Requires clean up and/or fixing; evidence of incident remains **Payload:** Small damage prevents system from functioning as designed, but still mostly functional
IV	Minor	**Personnel:** Minor abrasions and contusions **Environment:** Requires clean up and/or fixing; no lasting effects **Payload:** Introduces small amount of variance in performance
V	Insignificant	**Personnel:** Temporary confusion, bewilderment, or discomfort **Environment:** Little or no damage; easily cleaned up or fixed with no lasting effects **Payload:** Nominal performance regardless of incident

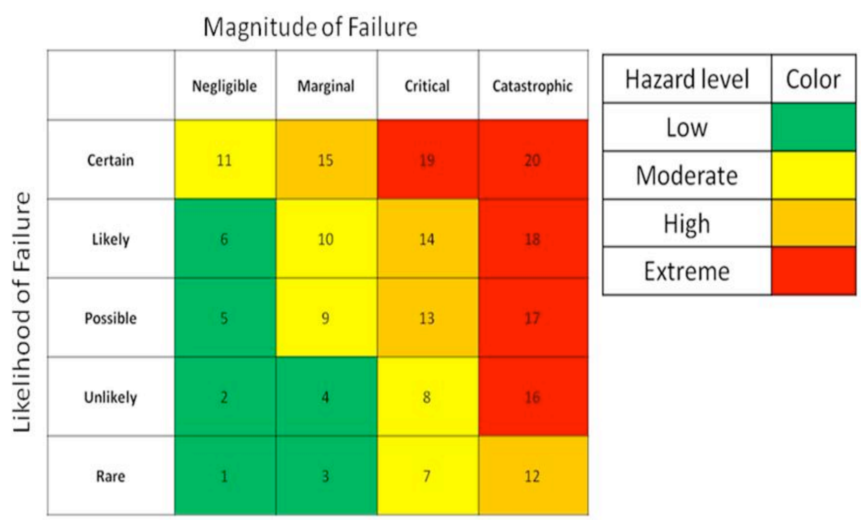

Figure 3. Hazard Assessment Matrix.

D. Concept of Operations

A key enabler a successful design is to development of a well-defined Concept of Operations (CONOPS). The CONOPS clearly defines operational concepts in a single figure, and allows an independent audience to understand the primary design and operation theory at a glance. The CONOPS allows subsystem design teams to scope the required levels of efforts very early in the program. Once established, the CONOPS should not be modified unless the program reaches a clear design or operational limit.

One of the "*hard and fast*" rules of the USLI competition is that launch teams must use a National Association of Rocketry (NAR) certified[4] commercially available, hobby rocket motor for the main boost-element of the vehicle. Hobby rocket motors are not as well characterized as military or NASA-certified motors, and the manfacturer's specifications for total impulse among a particular type or class of motors can vary by as much as 20%. An impulse variability of 20% results in an apogee altitude error in excess of 300 meters. Consequently, the USU Chimaera team concluded that a closed-loop energy management system was required to "hit" the desired target-altitude at an accuracy level that is competitive to win the USLI competition.

Previous USU entries into the USLI competition solved this problem with a closed-loop energy management system that used air brakes to modulate the total energy of the rocket. The previous design philosophy was to "*aim high and bleed energy*" using four deployable and retractable airbrakes mounted near the rocket boat tail. The brakes were deployed at prescribed waypoints, and the energy management system running on the onboard avionics computer determined the deployment times. The target total energy-state is approached asymptotically from above. Because of newly established launch-range safety restrictions, the USLI scoring rubric for the altitude prize has been significantly modified to severely penalize teams that exceed the one mile altitude limit. Furthermore, any rocket exceeding the target altitude by *more than 100 meters will be disqualified from the competition.* Thus the previous "*aim high*" strategy is far too risky with regard to the competition rules, and has been being replaced by an "*aim low and boost energy*" strategy.

Figure 4 shows the revised concept of operations for this vehicle. The airbrakes are replaced with small aerospike-based thrusters, and energy is added instead of depleted. The design uses an L-class solid rocket motor to boost the launch vehicle to a projected altitude 50-150 meters below the one-mile target. Following the main motor burnout, two small cold-gas aerospike thrusters are operated to augment the vehicle energy level. A closed-loop algorithm calculates and manages the vehicle energy by pulsing the cold-gas thrusters. This approach allows the target altitude to be approached asymptotically from below. The cold-gas base-area bleed augmentation system was designated by the acronym C-BAS, and for the remainder of this paper that designation will be used.

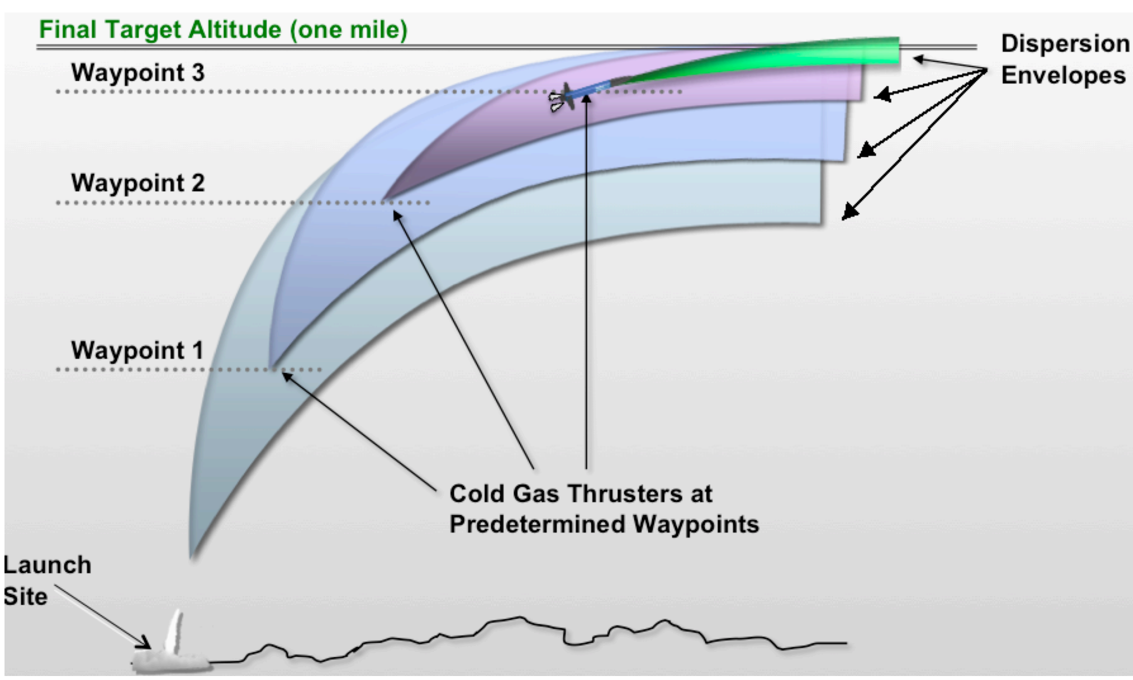

Figure 4. Energy Management, Concept of Operations.

Figure 5 shows flight simulation results comparing a typical un-augment ballistic trajectory against a trajectory with C-BAS energy management active. The un-augmented ballistic trajectory reaches an apogee of approximately 1500 meters above the launch ground level. In the augmented trajectory as soon as the vehicle drag, predicted by the axial deceleration level, drops below the nominal C-BAS thrust-level the C-BAS system is activated. Based up on the best knowledge of the vehicle performance parameters, flight simulations predict that the nominal C-BAS activation event occurs at an altitude of approximately 900 meters above the ground level and 7.5 seconds into the flight. Once activated the C-BAS operates continuously to compensate for any defect in the post-burnout energy level. Once the vehicle energy reaches the desired level, the C-BAS system is pulsed to negate the effects of drag and "trims" the desired flight energy level. The USLI rules specifically prohibit forward thrusting devices, thus no mechanism for attenuating energy in the event that the rocket has excessive energy was available with the C-BAS system. A detailed description of the C-BAS system hardware is presented in *Payload Overview* and *Avionics* sub-sections of this report. A detailed description of the vehicle energy management algorithm is presented in *Energy Management* section of this report.

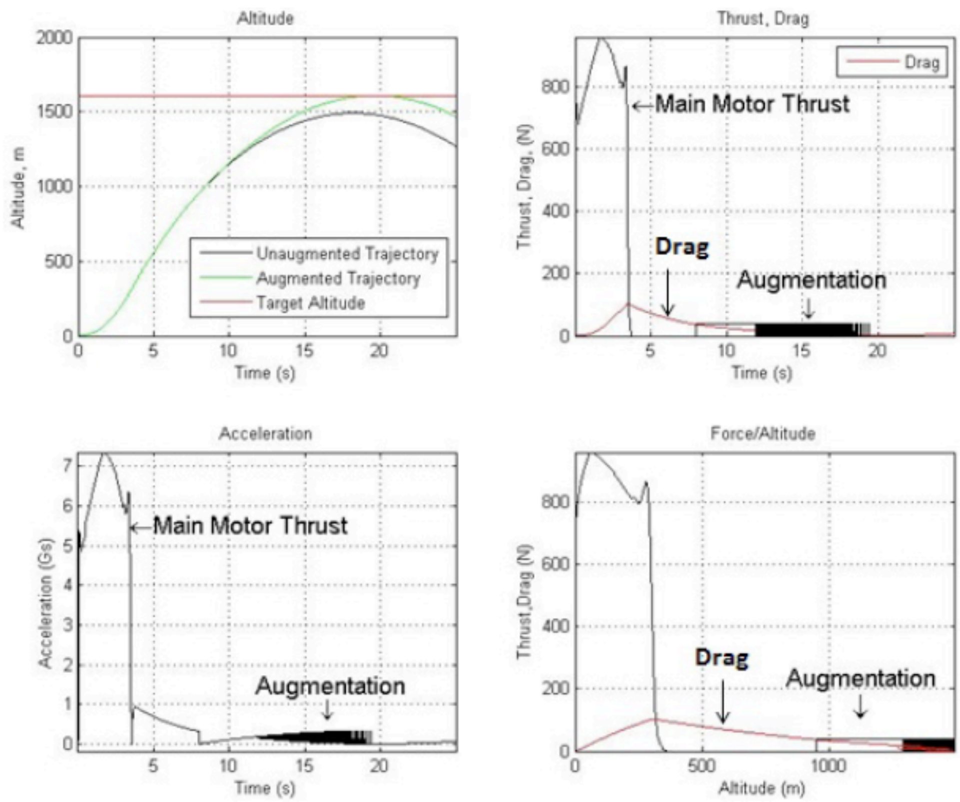

Figure 5. Comparison of Augmented and Ballistic Flight Trajectories.

E. Motor Selection Trade Study

Figure 6 depicts the systems-engineering process that was used to select the main power plant for the rocket and the working fluid for the cold-gas thruster sub-systems. As described in the previous section the majority of the flight impulse was delivered by a commercially available solid propelled high-powered rocket motor. The cold-gas augmentation system is used to "trim" the energy level of the vehicle. For this trade study every commercially certified high-powered rocket with at least an L-class (Ref. 4) impulse was examined. An L-class impulse motor allows impulse ranges from *2560 N-s* to *5120 N-s*. Thrust and impulse data were obtained from the NAR-supported website "Thrustcurve.org."[5]

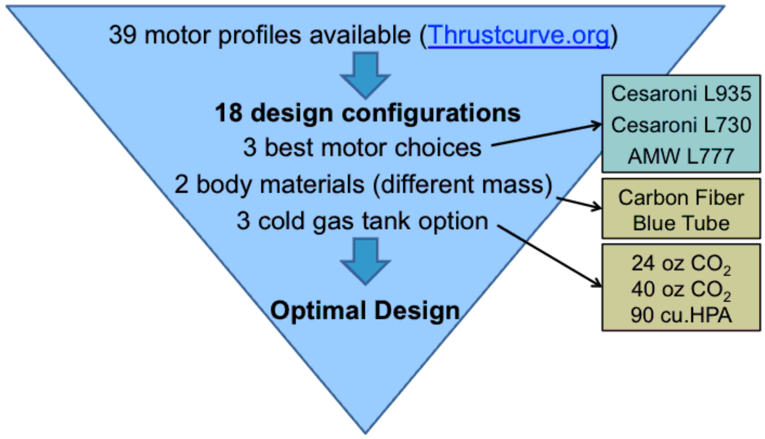

Figure 6. Systems Engineering Process Used to Select Main Motor and Cold-Gas Working Fluid.

Table 4 lists the properties of the down-selected Cesaroni L-730[6] solid rocket motor. The Cesaroni is classified by NAR as an L-impulse class rocket, and is reusable. The external motor case is constructed of aluminum, with a phenolic insulating sleeve. The reloadable fuel grain consists of 6 "Bates" fuel grain segments with each segment approximately 10 cm in length. Total propellant for each reload is 1.351 *kg*, and the loaded motor mass is 2.247 *kg*. The accompanying phenolic nozzle is designed for a single use. The nozzle has a conical design, the nominal throat area is 1.90 cm^2, and the nominal expansion ratio is 3.25.

Table 4. Cesaroni L-730 Solid Rocket Motor Properties

Motor case Diameter / Length	*54mm / 64.9 cm*
Average Thrust / Burn Time	*730 N / 3.8 s*
Total Impulse / Effective Specific Impulse, I_{sp}	*2765 N-s/ 209 s*
Nozzle Throat Area / Expansion ratio	$1.90\ cm^2$ / *3.25*
Cost per Reload	*$160*

Two options were investigated for the cold-gas augmentation system, carbon dioxide (CO_2), and high-pressure air (HPA). Even though HPA has a higher I_{sp} than CO_2, the higher HPA component weights resulted in unsatisfactory propellant mass fractions and volumes, and in the end carbon dioxide was selected as the working fluid. Mandating that the nominal thrust of the C-BAS exceeds the drag of the vehicle before operation insures that the fluid leaving the tank exit is liquid. Insuring a liquid tank exit state minimizes thrust variability and tank pressure drop due cooling as vapor state fluid exist the tank. Details of the cold-gas augmentation system (C-BAS) will be presented in the *Final Design* section of this report.

IV. Final Vehicle Design Description

This section presents only the final design for the vehicle, dubbed "the Javelin" by the Chimaera team. The design evolution and details regarding the subsystem verification testing used to characterize the component performances can be found in the student design review documents submitted to NASA.[7] Key ground and flight test results will be presented later *Results and Discussion* section of this paper. Detailed descriptions of the test facilities and instrumentation will not be presented.

A. Vehicle Overview

Figure 7 shows the overall vehicle dimensions. Figure 8 shows the vehicle mass breakdown. The Javelin has a total launch mass of *12.59 kg*, and has a tip-to-tail length of *225 cm*. The aft section of the rocket houses the Cesaroni L730 solid propellant motor and C-BAS payload. Both the solid motor and C-BAS were tested extensively to verify that available impulse levels are sufficient to meet mission objectives. A 25 cm bay located behind the rocket nosecone houses all flight avionics. The avionics suite includes an inertial measurement unit (IMU), two pressure-based altimeters, and a three-axis magnetometer. Navigation data are processed in a small, on-board flight computer. The flight computer executes a Kalman filtering algorithm that continuously estimates the vehicle acceleration, altitude, velocity, orientation, angular rates, flight path angle, and heading. These flight trajectory estimates are used to calculate the total specific energy and potential altitude of the vehicle. The flight computer also activates and operates the energy management system hardware.

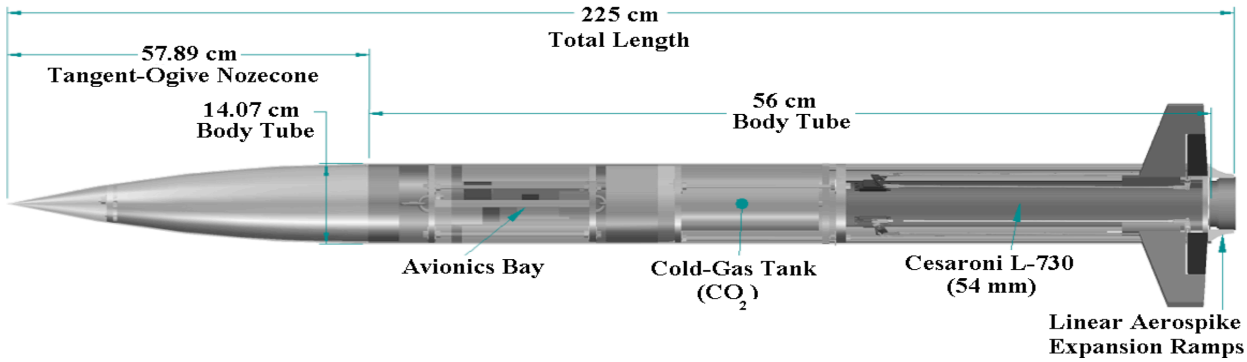

Figure 7. Basic Vehicle Dimensions.

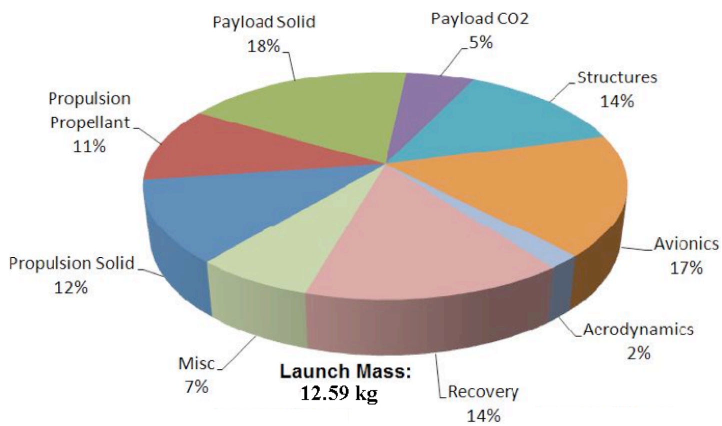

Figure 8. Vehicle Mass Breakdown.

The Javelin launches on a student-built mobile system featuring a 4.5-meter aluminum truss-launch rail. This mobile system serves as a transport trailer for the rocket and support equipment and acts as a base for the launch platform. The launch rail is an integral part of the trailer used to transport the Javelin. Adjustable jacks on the mobile launch platform allow the orientation of the launch rail to be adjusted to the desired condition. For the USLI launch competition flights, the rail orientation was adjusted at a 90^o pitch angle in order to maximize the apogee altitude for a given launch energy level. Figure 9a shows the launch operations team mounting a rocket on the mobile launch platform rail. The rocket launch is initiated using an industry-standard remote controller design. Figure 9b shows the components and electronic circuit design for the student-built launch controller.

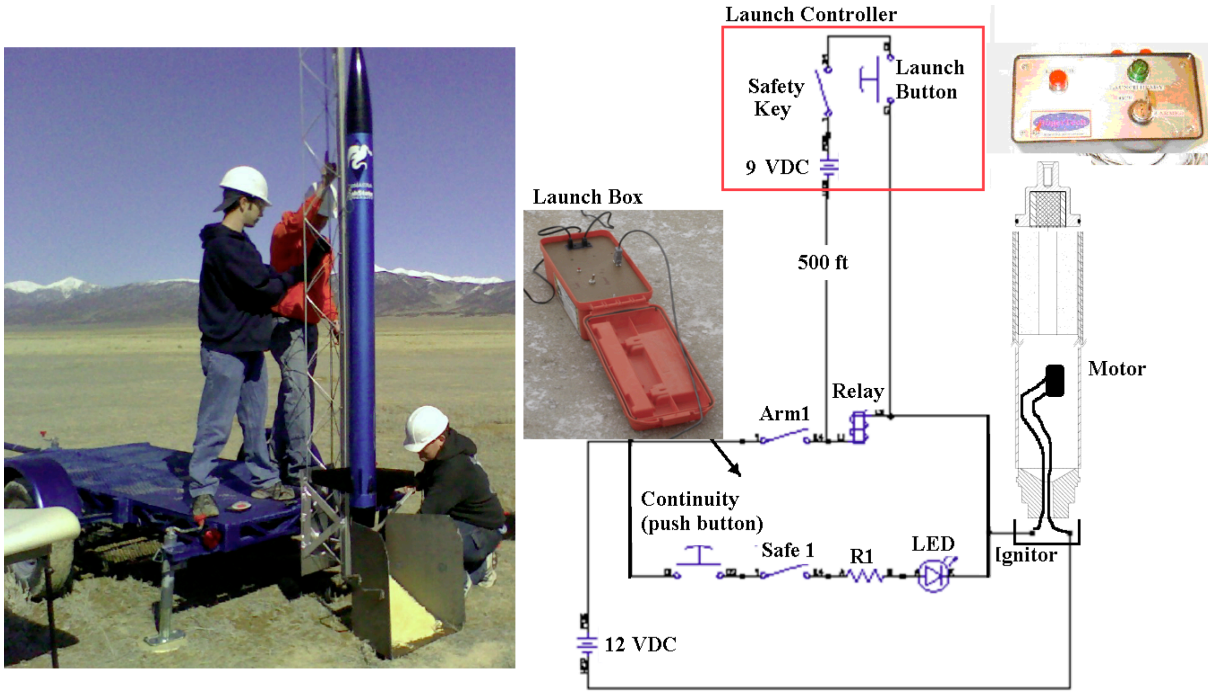

a) Launch Rail

b) Launch Box, Ignitor, and Controller

Figure 9. Mobile Launch Platform Features.

Two pressure altimeters are used for dual, redundant deployment of the recovery system's parachutes. One of the altimeters was also designated to provide the official altitude measurement for the USLI competition. The avionics suite will be discussed in detail in later in this section of the document of this design document. The rocket body was constructed from Blue Tube 2.0®.[8] Blue Tube is an extremely lightweight and durable vulcanized-rubber reinforced phenolic material designed for amateur rocketry use. Blue Tube 2.0® costs approximately 1/3rd as much as carbon fiber reinforced composite. The material was tested and demonstrated capable of withstanding the maximum loads encountered during flight. The vehicle was stabilized using three fixed tapered-rectangular fins constructed from a honeycomb fiberglass composite. The recovery system features a dual redundant deployment system using nylon parachutes with Kevlar harnesses sized to keep the descent rate within ranges mandated by USLI competition rules. The drogue parachute is 76 cm in diameter and the main parachute is 305 cm in diameter.

B. Payload Overview

As described previously in the *Systems Engineering* section, the primary vehicle payload is a cold-gas energy management system whose external contour is derived from aerospike nozzle theory. The aerospike-derived isentropic expansion ramps are wrapped around the primary solid motor core. This concentric thruster design fits entirely within the main rocket body tube, and when compared to "strap-on" thrusters, adds negligible aerodynamic drag to the external configuration. Figure 10 depicts the integration of the cold-gas thruster ramps thrusters into the rocket base area. The external expansion ramp contour was designed to allow an isentropic expansion from the operating plenum pressure to external ambient pressure conditions. The method developed by Lee and Thompson,[9] modified for a 2-dimensional sonic exit condition was used to design the spike contour. Each spike had an expansion ramp width of 1.5 cm, a length of 4.4 cm, and a throat exit area of approximately 0.072 cm^2. The entire thruster was approximately 6.6 cm in length. Side fences were used to limit the lateral expansion of the plume and the resulting thrust loss.[10] The ramps were truncated at 85% of their theoretical length. When operated at 850 kPa (120 psig) plenum pressure the combined system was designed to produce a nominal thrust of approximately 10 Newtons.

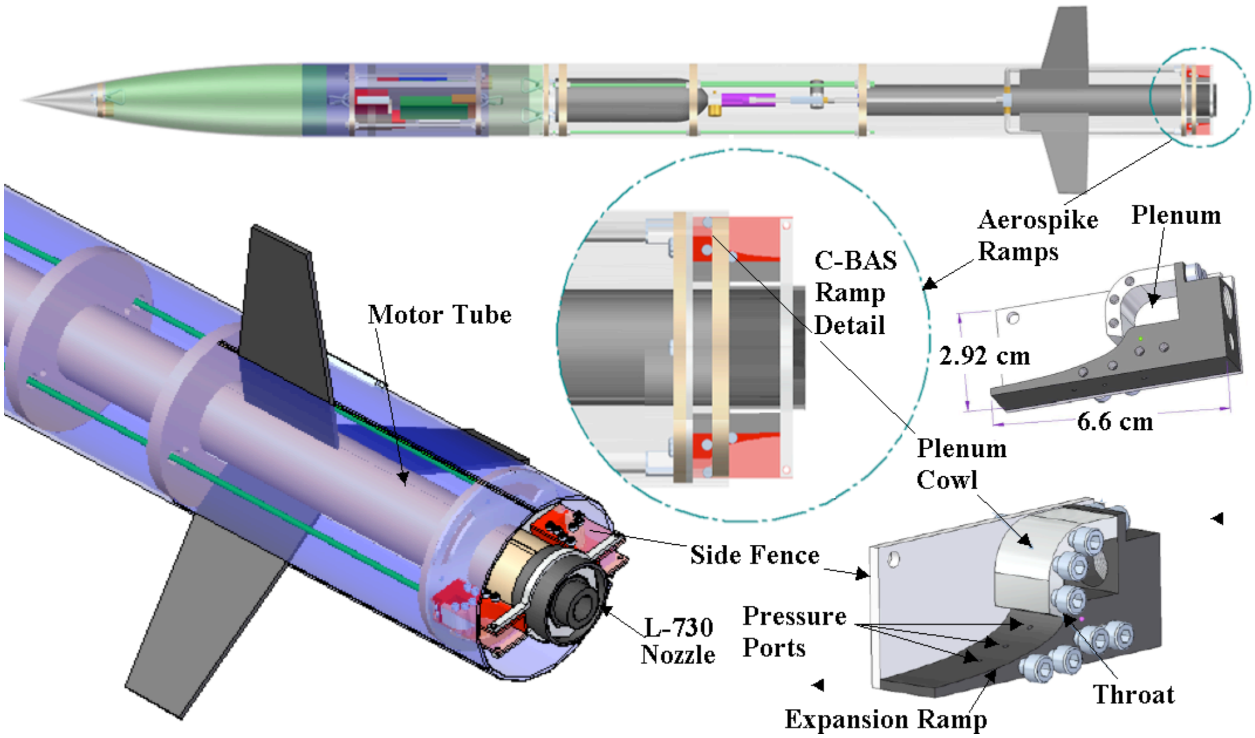

Figure 10: Integration of Aerospike Thrusters into Vehicle Base Area.

Figure 11 depicts the propellant feed system for the augmentation thrusters. The pneumatic components (Figure 11a) consist of the CO_2 tank, pressure regulator, solenoid valve, steel-mesh propellant feed tubing, and the aerospike thrusters. The in-line regulator has an output pressure that is variable from 450 psig (3200 kPa) to 80 psig (640 kPa). This regulator drops the flow from saturation pressure in the tank, approximately 5000 kPa, to the design operating pressure, approximately 1250 kPa. Pressure regulation is used to insure that a constant plenum feed pressure was available for C-BAS operation,/ Constant feed pressure allows a more consistent thrust level. Standard paintball-class tanks carry the onboard CO_2 in a saturated-liquid form. Interchangeable options for both 24 oz (0.68 1 kg) and 12 oz (0.34 kg) CO_2 tank sizes are provided for in the design. Additional flight instruments include 6 C-BAS expansion ramp surface pressure transducers. The pressure ports are located on each ramp 1, 2, and 3 cm aft of the C-BAS thruster throat exit. A separate inexpensive R-DAS[11] (Rocket data Acquisition System) system was flown to log the ramp pressures. Figure 11a shows the CO_2 tank, regulator, and solenoid valve mounted in the body tube near the vehicle mid-deck.

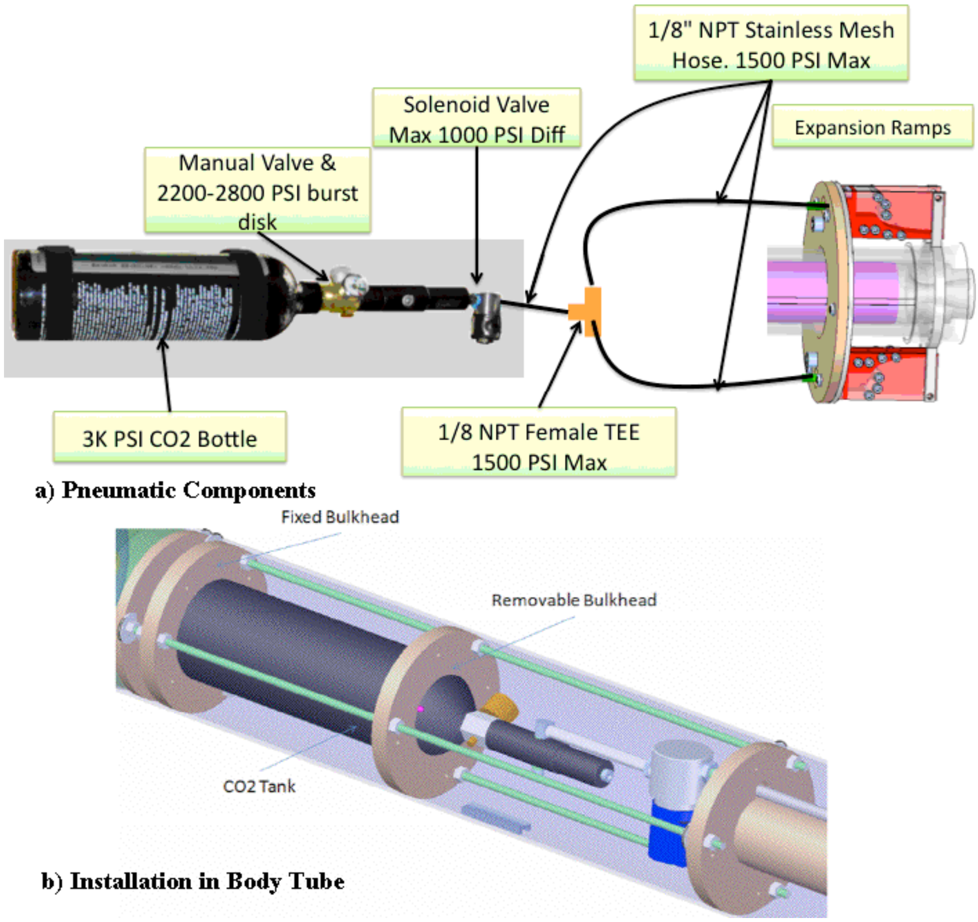

Figure 11: Pneumatic Component Layout of Cold-gas Aerospike Thrusters.

C. Avionics

A suite of onboard instruments was carried to measure the vehicle trajectory and manage the flight systems. Navigation sensors include an inertial measurement unit (IMU), a pressure-pressure based altimeter, and a single-axis magnetometer. Figure 12 shows the avionics systems components (Figure 12a) and a functional block diagram (Figure 12b). Navigation data are processed in a small onboard avionics computer using a Kalman-filter to continuously estimate the total specific energy and potential altitude of the vehicle. The primary onboard navigation instrument is miniature inertial measurement unit (IMU) built by Micro-Strain®, Inc.[12] The IMU features a high-performance miniature attitude heading reference system that includes embedded tri-axial accelerometers, rate-gyros, magnetometers, and a temperature sensor. The form factor and weight are very small, and this device is mounted on the inner platform of the vehicle without significantly affecting the weight and inertia of the platform. The IMU sensor data is blended in an internal microprocessor running a sensor fusion algorithm to provide inertial navigation quality output parameters. User-selectable output parameters include Euler angles, rotation matrix components, velocity vector components, acceleration vector components, 3-axis angular rates, and 3-axis magnetic field components. The IMU data was complemented by ground-referenced altitude measurements from a pressure based PerfectFlite® Altimeter.[13] The R-DAS system is separate from the main avionics. Its only function is to log and store the aerospike ramp pressure data.

Onboard control law calculations, data flow management, and C-BAS activation are controlled using a GumStix® Overo-Tide micro-computer.[14] The GumStix is a 17 mm x 58 mm, 600 MHz single-board computer that features the open-source Overo development platform. A Ubiquiti® Bullet[15] 2HP WiFi transmitter/receiver provides communications between the onboard flight computer and a ground based laptop receiving station. The "Bullet" transmits using an industry standard IEEE 802.11 G[16] wireless telemetry link. A user datagram protocol (UDP) was used to packet the streaming downlink data. Options for a communications uplink were available but never implemented for this project. The ground-based laptop runs an interface program, written in the National Instruments Labview 2010® programming language[17] that allows direct control of all onboard functions including built-in test diagnostics, startup, and navigation algorithm startup settings. Finally this program receives and logs pertinent flight data including the cold-gas measurement parameters, IMU outputs, and system health bits.

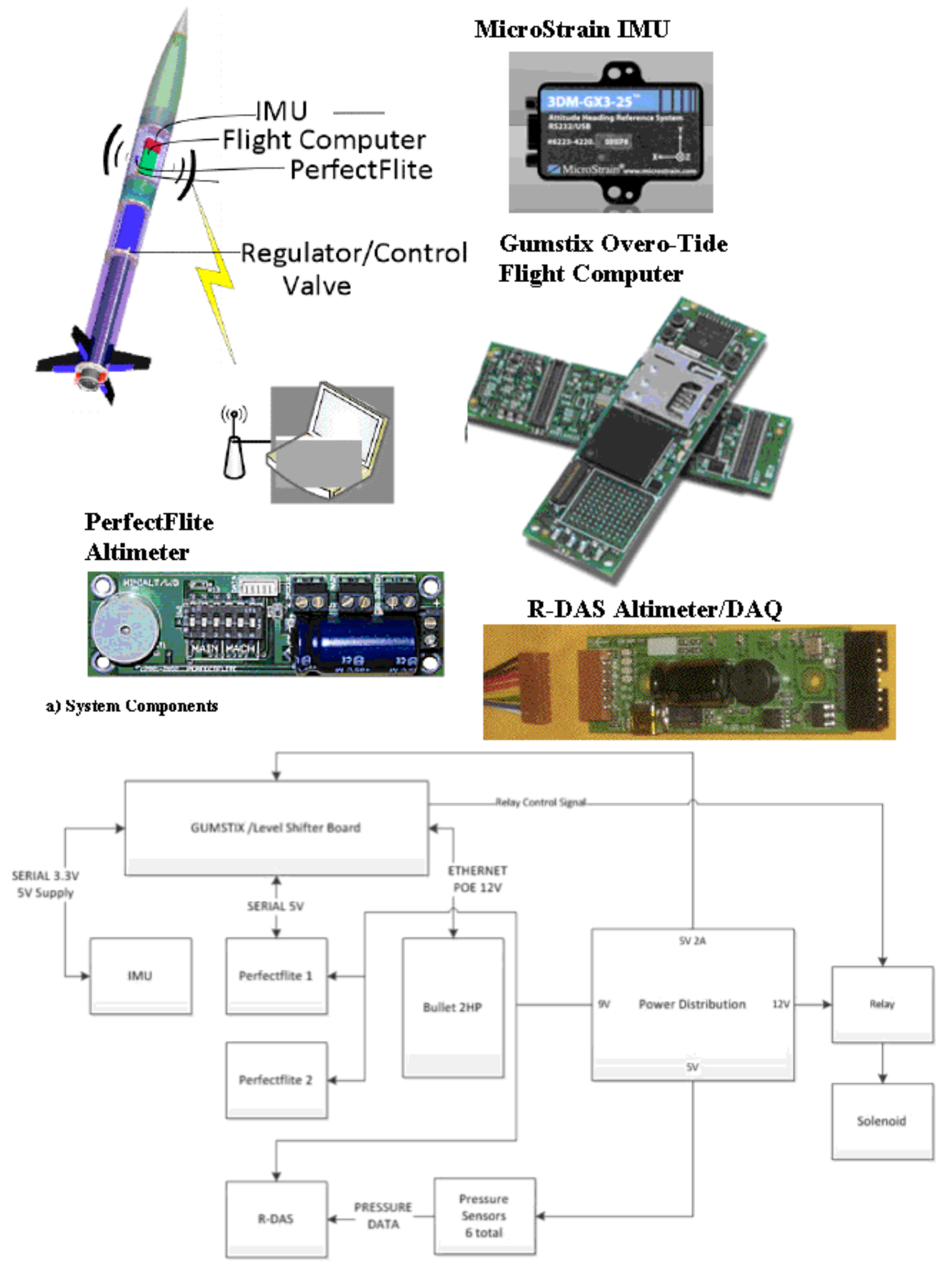

b) Functional Block Diagram

Figure 12. Avionics System Components and Functional Diagram.

D. Recovery System Design

As mentioned in the introduction to this section, the vehicle featured a dual-deployment (drogue/main) and dual-redundant recovery system. Figure 13 presents a functional bock diagram of the parachute deployment system. Two PerfectFlite altimeters were used to initiate deployment. The primary PerfectFlite sensor was also used to as a part of the avionics navigation suite and provided the "official" attitude measurement for the USLI competition. When either altimeter senses apogee, a signal is sent fire electronic matches, which in turn fire dual redundant black powder ejection charges. Gases generated by the black powder ejection charges separate the avionics bay from the main airframe and deploy the drogue parachute. To reduce drift, but slow the rocket enough for a safe landing, the main parachute is deployed at approximately *1000 ft (300 m)* AGL. Figure 13 shows the functional block diagram of the parachute deployment system. Table 5 lists the recover system design and operating parameters.

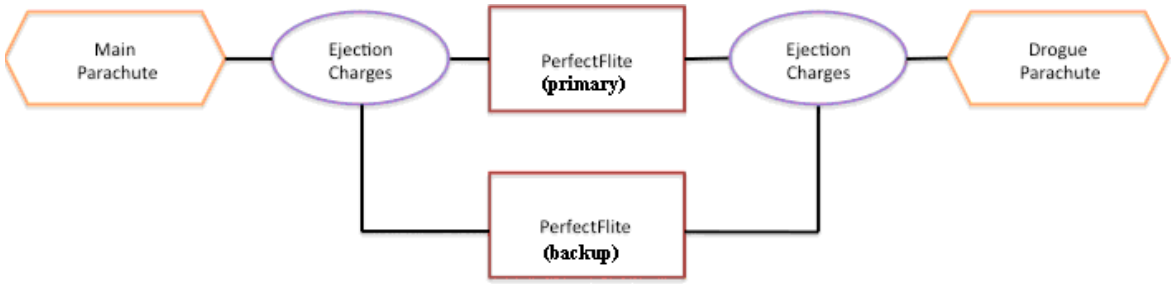

Figure 13. Functional Block Diagram of the Parachute Deployment System.

Table 5. Recovery System Design and Operating Parameters.

Parameter	Drogue Parachute	Main Parachute
Parachute Type	Conical	Conical
Deployment Altitude (*m AGL*)	5032	300
Deployment Air Density (kg/m^3)	1.031	1.163
Deployment Velocity (*m/s*)	42.58	22.26
Nominal Terminal Velocity (*m/s*)	23.65	5.64
Drag Coefficient	0.8	0.8
Reference Area (m^2)	58.85	884.96
Peak Opening Load (*N*)	583.77	526.38

V. Kalman Filter Navigation Equations

As mentioned in the introductory section, the IMU and altimeter data are used to calculate the vehicle trajectory parameters in real time, and these results are used to predict apogee based on the overall energy level of the vehicle. This section describes the vehicle dynamics and Kalman filtering equations used to estimate the vehicle trajectory in real time.

A. Kalman Filter State Equations

The discrete form of the Kalman filter equations are used for this application, with the state equations discretized using trapezoidal rule. The continuous-time state equation describing the translational dynamics of the vehicle[18] is

$$\begin{bmatrix} \dot{u} \\ \dot{v} \\ \dot{w} \\ \dot{h} \end{bmatrix} = \begin{bmatrix} 0 & r & -q & 0 \\ -r & 0 & p & 0 \\ q & -p & 0 & 0 \\ -M_{13} & -M_{23} & -M_{33} & -\dfrac{1}{\tau} \end{bmatrix} \cdot \begin{bmatrix} u \\ v \\ w \\ h \end{bmatrix} + g_0 \begin{bmatrix} A_x + \dfrac{g}{g_0} \cdot M_{13} \\ A_y + \dfrac{g}{g_0} \cdot M_{23} \\ A_z + \dfrac{g}{g_0} \cdot M_{33} \\ 0 \end{bmatrix} \tag{1}$$

Equation (1) is written in matrix form as

$$\dot{x} = A \cdot x + B \cdot u$$

$$\rightarrow x = \begin{bmatrix} u \\ v \\ w \\ h \end{bmatrix}, \quad A = \begin{bmatrix} 0 & r & -q & 0 \\ -r & 0 & p & 0 \\ q & -p & 0 & 0 \\ -M_{13} & -M_{23} & -M_{33} & -\frac{1}{\tau} \end{bmatrix}, \quad B \cdot u = g_0 \begin{bmatrix} A_x + \frac{g}{g_0} M_{13} \\ A_y + \frac{g}{g_0} M_{23} \\ A_z + \frac{g}{g_0} M_{33} \\ 0 \end{bmatrix}. \qquad (2$$

In Eq. (2) M is the direction cosine matrix given by

$$\overleftrightarrow{M} = \left\{ M_{ij} \right\} =$$

$$\begin{bmatrix} \cos\theta\cos\psi & \cos\theta\sin\psi & -\sin\theta \\ \sin\phi\sin\theta\cos\psi - \cos\phi\sin\psi & \sin\phi\sin\theta\sin\psi + \cos\phi\cos\psi & \sin\phi\cos\theta \\ \cos\phi\sin\theta\cos\psi + \sin\phi\sin\psi & \cos\phi\sin\theta\sin\psi - \sin\phi\cos\psi & \cos\phi\cos\theta \end{bmatrix}. \qquad (3$$

When Eq. (2) is discretized via trapezoidal rule where both the current and previous frame IMU data are used to approximate the derivatives,

$$\begin{aligned} \tilde{x}_{k+1} &= \left[I + A_k \cdot \Delta t \right] \cdot x_{k/k} + \Delta t \left(B \cdot u \right)_k \\ \tilde{\dot{x}}_{k+1} &= A_{k+1} \cdot \tilde{x}_{k+1} + \left(B \cdot u \right)_{k+1} \end{aligned}, \qquad (4$$

the result is

$$x_{k+1/k} = x_{k/k} + \frac{\Delta t}{2} \left[\left(A_{k+1} \cdot \tilde{x}_{k+1} + \left(B \cdot u \right)_{k+1} \right) + \left(A_k \cdot x_k + \left(B \cdot u \right)_k \right) \right] \qquad (5$$

The state equation is assumed to be contaminated by additive, gasssian-distributed white noise. This noise has a covariance represented by the matrix $Q_{k+1.}$ A model for the state noise covariance will be developed later in this section.

B. Observation Equations

When the sensed acceleration measurements are integrated “open-loop”, the velocity and subsequent altitude estimates will drift with time, and a stable altitude measurement is needed to minimize this drift. For this application to PerfectFlite® altitude measurement is used to stabilize the integration. Since the PerfectFlite data provides the “judged altitude,” for the USLI competition, initially the perfect flight data will be weighted moderately by the Kalman filter equations; but as apogee is approach it will be increasingly weighted more heavily. This scheme, to be described in detail later in this section, has the effect of making the altimeter the “truth” data for the filter apogee prediction. The resulting observation equation is

$$\left[h_{PerfectFlite} \right] = \begin{bmatrix} 0 & 0 & 0 & 1 \end{bmatrix} \begin{bmatrix} u \\ v \\ w \\ h \end{bmatrix}, \qquad (6$$

where the $[u\ v\ w\ h]^T$ is the current state vector estimate. The measurement matrix C, has an invariant form

$$C = \begin{bmatrix} 0 & 0 & 0 & 1 \end{bmatrix}. \qquad (7$$

Since the order of the measurement vector is 1, the measurement noise variance R_{k+1}, is a scalar quantity. A model for the measurement noise variance will be developed later in this document.

C. State Covariance Propagation Using Explicit Euler Rule

A simple Explicit Euler discretization algorithm uses only the current IMU data for the covariance propagation. This approach allows the covariance update to be performed without requiring real time matrix inversion. The discretization is

$$\frac{x_{k+1} - x_k}{\Delta t} = A_k \cdot x_k + \left(B \cdot u\right)_k \rightarrow x_{k+1} = \left[I + A_{k+1} \cdot \Delta t\right] \cdot x_k + \Delta t\left(B \cdot u\right)_k$$
$$\boxed{x_{k+1} = \left[I + A_k \cdot \Delta t\right] \cdot x_k + \Delta t\left(B \cdot u\right)_k} \quad . \tag{8}$$

The approximate state transition matrix is

$$\Phi_{k+1} = \left[I + A_k \cdot \Delta t\right] = \begin{bmatrix} 1 & r \cdot \Delta t & -q \cdot \Delta t & 0 \\ -r \cdot \Delta t & 1 & p \cdot \Delta t & 0 \\ q \cdot \Delta t & -p \cdot \Delta t & 1 & 0 \\ -M_{13} \cdot \Delta t & -M_{23} \cdot \Delta t & -M_{33} \cdot \Delta t & 1 - \dfrac{\Delta t}{\tau} \cdot \end{bmatrix} . \tag{9}$$

The state transition matrix of Eq. (8) is used to propagate the state covariance assuming additive state noise with covariance $Q_{k+1.}$ The resulting state covariance prediction equations is

$$P_{k+1/k} = \Phi_{k+1} P_{k+1/k} \Phi_{k+1}{}^T + Q_{k+1} \tag{10}$$

D. Kalman Gain Matrix

The Standard form of the Kalman gain matrix is

$$K_{k+1} = P_{k+1/k} C^T \left[C P_{k+1/k} C^T + R_{k+1}\right]^{-1} . \tag{11}$$

Substituting in for the actual "*C*" matrix (Eq. (7)) the inverse term becomes

$$C P_{k+1/k} C^T + R_{k+1} = \begin{bmatrix} 0 & 0 & 0 & 1 \end{bmatrix} \cdot \begin{bmatrix} P_{11} & P_{12} & P_{13} & P_{14} \\ P_{21} & P_{22} & P_{23} & P_{24} \\ P_{31} & P_{32} & P_{33} & P_{34} \\ P_{41} & P_{42} & P_{43} & P_{44} \end{bmatrix} \cdot \begin{bmatrix} 0 \\ 0 \\ 0 \\ 1 \end{bmatrix} + R_{k+1} = \begin{bmatrix} 0 & 0 & 0 & 1 \end{bmatrix} \cdot \begin{bmatrix} P_{14} \\ P_{24} \\ P_{34} \\ P_{44} \end{bmatrix} + R_{k+1} = P_{44} + R_{k+1} . \tag{12}$$

Expanding and collecting terms, the flight-implemented Kalman gain matrix becomes

$$K_{k+1} = P_{k+1/k} C^T \left[C P_{k+1/k} C^T + R_{k+1}\right]^{-1} = \begin{bmatrix} \dfrac{P_{14}}{P_{44} + R_{k+1}} \\ \dfrac{P_{24}}{P_{44} + R_{k+1}} \\ \dfrac{P_{34}}{P_{44} + R_{k+1}} \\ \dfrac{P_{44}}{P_{44} + R_{k+1}} \end{bmatrix}_{k+1/k} . \tag{12}$$

E. Kalman Update Equations

The standard form of the Kalman state update equation is

$$\hat{x}_{k+1/k+1} = \hat{x}_{k+1/k} + K_{k+1} \cdot \left[Z_{k+1} - C \cdot \hat{x}_{k+1/k} \right]. \qquad (13$$

Substituting ifor K_{k+1} and C gives

$$\begin{bmatrix} u \\ v \\ w \\ h \end{bmatrix}_{k+1/k+1} = \begin{bmatrix} u \\ v \\ w \\ h \end{bmatrix}_{k+1/k} + \begin{bmatrix} \frac{P_{14}}{P_{44}+R_{k+1}} \\ \frac{P_{24}}{P_{44}+R_{k+1}} \\ \frac{P_{34}}{P_{44}+R_{k+1}} \\ \frac{P_{44}}{P_{44}+R_{k+1}} \end{bmatrix}_{k+1/k} \left(h_{PerfectFlite\ k+1} - \hat{h}_{k+1/k} \right) \qquad (14$$

The standard form of the covariance update equation is

$$P_{k+1/k+1} = \left[I - K_{k+1} \cdot C \right] P_{k+1/k}. \qquad (15$$

Substituting for K_{k+1} and C gives the flight-implemented form of the covariance update equation

$$P_{k+1/k+1} = \left[\begin{bmatrix} 1 & 0 & 0 & 0 \\ 0 & 1 & 0 & 0 \\ 0 & 0 & 1 & 0 \\ 0 & 0 & 0 & 1 \end{bmatrix} - \begin{bmatrix} \frac{P_{14}}{P_{44}+R_{k+1}} \\ \frac{P_{24}}{P_{44}+R_{k+1}} \\ \frac{P_{34}}{P_{44}+R_{k+1}} \\ \frac{P_{44}}{P_{44}+R_{k+1}} \end{bmatrix}_{k+1/k} \begin{bmatrix} 0 & 0 & 0 & 1 \end{bmatrix} \right] P_{k+1/k} = \begin{bmatrix} 1 & 0 & 0 & \frac{-P_{14}}{P_{44}+R_{k+1}} \\ 0 & 1 & 0 & \frac{-P_{24}}{P_{44}+R_{k+1}} \\ 0 & 0 & 1 & \frac{-P_{34}}{P_{44}+R_{k+1}} \\ 0 & 0 & 0 & 1-\frac{P_{44}}{P_{44}+R_{k+1}} \end{bmatrix} P_{k+1/k} \qquad (16$$

F. State Noise Covariance Model

As described earlier the state noise (Q_{k+1}) and measurement error *(R_{k+1})* covariance models are necessary to complete the filtering algorithm. The state equation covariance model is derived from errors in the input data from the IMU measurements. The dominant error in the state equation results from the noise in the accelerometer and pitch angle measurements. Altitude errors due to roll and yaw angle are negligible. Additionally, cross axis errors are assumed to be negligible and all off-diagonal covariance terms are set to zero. Along a ballistic trajectory the angle of attack is small and $u >> \{v, w\}$, thus

$$\dot{h} = \sin\theta \cdot u - \sin\phi \cos\theta \cdot v - \cos\phi \cos\theta \cdot w. \qquad (17$$

The altitude rate error due to IMU attitude errors can be approximated by

$$\delta\dot{h} = V \cdot \cos\theta \cdot \delta\theta \qquad (18$$

and

$$V \cdot \cos\theta \approx V_{horizontal}. \qquad (19$$

As will be presented later in the *Energy Management* section, following motor burnout for a ballistic trajectory the horizontal velocity remains approximately constant throughout the flight. The discrete variance is then approximated by

$$\sigma^2 h \approx \Delta t^2 \left(V \cdot \cos\theta\right)^2 \cdot \sigma^2{}_{\theta} = \Delta t^2 \cdot V_{horizontal}{}^2 \cdot \sigma^2{}_{\theta} \tag{20}$$

The resulting state noise covariance model is

$$Q_{k+1} = \left(\Delta t \cdot g_0\right)^2 \begin{bmatrix} \sigma^2{}_{A_x} & 0 & 0 & 0 \\ 0 & \sigma^2{}_{A_y} & 0 & 0 \\ 0 & 0 & \sigma^2{}_{A_z} & 0 \\ 0 & 0 & 0 & \left(\dfrac{V_{horizontal}}{g_0}\right)^2 \sigma^2{}_{\theta} \end{bmatrix}. \tag{21}$$

The first three parameters along the matrix diagonal represent the variances due to the IMU accelerometer uncertainties (*g's*^{2}), and the final parameter on the diagonal models the altitude variance due to the IMU attitude errors. Table 6 summarizes the expected IMU[19] Accelerometer, pitch attitude, and altitude-rate errors.

Table 6. Summary of Expected IMU Sensor Errors

$V_{horizontal}$, *m/sec*	$\{\sigma_{Ax},\sigma_{Ay},\sigma_{Az}\}(g's)$	σ_θ (*deg,radians*)	$\dfrac{V_{horizontal}}{g}\sigma_\theta$ (s)
0	*±0.10 g's*	*±2 deg. (0.035 rad)*	*0.000 sec*
10	-	-	*0.036 sec*
20	-	-	*0.072 sec*
30	-	-	*0.107 sec*
40	-	-	*0.142 sec*
50	-	-	*0.178 sec*

F. Measurement Noise Covariance Model

The measurement error covariance model is calculated directly from the expected uncertainty in the *PerfectFlite* altitude measurement. The stated accuracy of the altitude measurement is +0.25-5% of reading.[20] This value equates to approximately *±4-8 meters* measurement uncertainty at apogee. Because the PerfectFlite reading is judged to be the "truth" metric for altitude in the competition, the variance will be linearly diminished with time so that the filter weights the sensor altitude reading more and more heavily as apogee is approached. Thus the potential altitude output used to control the vehicle's energy level will be strongly tied to the perfect flight altitude reading. The prescribed adaptive weighting function for the PerfectFlite measurement noise is

$$\sigma_{h_{PerfectFlite}} = \pm 0.005 \cdot \widehat{h}_{k/k} \cdot \left(1 - \frac{\widehat{h}_{k/k}}{h_{target}}\right) + \varepsilon \tag{22}$$

In Eq. 22 h_{target} is the target altitude of 1609.32 meters, $h_{k/k}$ is the current altitude estimate of the Kalman filter, and parameter ε is a small positive magnitude factor that prevents the measurement noise covariance from becoming *exactly zero* -- an event that would cause stability problems with the Kalman filter covariance propagation. Figure 14 plots the time-of-fight profile of Eq. (22) along a nominal flight trajectory. The minimum weighting (inverse of the error function) occurs shortly after motor burnout and approaches maximum value just prior to reaching apogee. The "ε" safety-factor was set to 0.1 meter for this calculation.

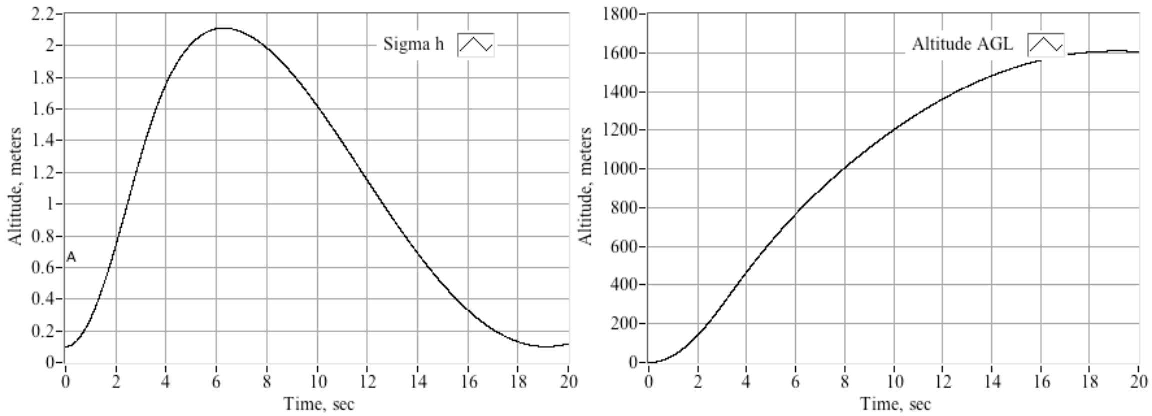

Figure 14. Time-of-Flight Profile for Measurement Noise Weighting Function.

VI. Energy Management Algorithm

The energy management algorithm uses a balance of potential and kinetic energy to predict the vehicle apogee altitude based on Kalman filter estimates of 1/2 the squared velocity (*kinetic energy per unit mass*) and altitude (*potential energy per unit mass*). The feedback algorithm checks calculated potential altitude against a target reference. If the energy state of the vehicle is low, the algorithm commands the flight avionics to activate the energy management system by opening the CO_2 solenoid valve. When the energy state climbs to the prescribed value, the solenoid valve closes.

A. Calculating the Potential Apogee Altitude

Key to the energy management described in the previous section is the "potential altitude" of the vehicle; derived from the sum of the gravitational potential energy and kinetic energy in the vertical direction. The potential altitude can be calculated using the body axis velocity and altitude estimates from the Kalman filtering algorithm. At any point along the trajectory the sum of the mass-specific potential energy is given by

$$\left(\frac{E}{m}\right)_{total} = g \cdot h + \frac{V^2}{2} \quad . \tag{23}$$

The total specific energy at apogee is related to the energy at any time following motor burnout by

$$\left(\frac{E}{m}\right)_{apogee} = g \cdot h_{apogee} + \frac{\left(V \cdot \sin\gamma\right)^2}{2} - \int_{t}^{t_{apogee}} \left(\frac{1}{2} \cdot \rho \cdot V^2\right) \cdot \left(\frac{C_D \cdot A_{ref}}{m \cdot g}\right) \cdot V \cdot dt \quad . \tag{24}$$

The last term on the right hand side of Eq. (24) is the energy depleted by drag forces acting on the rocket. For ballistic trajectories with a nearly vertical initial launch angle, the horizontal velocity of the rocket at motor burnout remains nearly constant throughout the climb to altitude, and Eq. (24) can be rearranged to predict the rocket's apogee altitude based on the energy state (*potential* + *kinetic energy*) estimated at any point along the trajectory

$$h_{apogee} = h(t) + \frac{\left(V(t) \cdot \sin\gamma\right)^2}{2 \cdot g} - \int_{t}^{t_{apogee}} \left(\frac{1}{2}\rho V^2\right) \cdot \left(\frac{C_D \cdot A_{ref}}{m \cdot g}\right) \cdot V \cdot dt \quad . \tag{25}$$

Near apogee the drag term in Eq. (25) diminishes, and the "near apogee" potential altitude calculation becomes

$$h_{potential} = h(t) + \frac{\left(V(t) \cdot \sin\gamma\right)^2}{2 \cdot g} \quad , \tag{26}$$

The available change in potential altitude equals the change in velocity resulting when a given mass of propellant is consumed. When the vehicle velocity is modified by an amount ΔV, then the corresponding change in kinetic energy per unit mass is

$$\frac{\Delta_{KE}}{m} = \frac{(V + \Delta V)^2 - V^2}{2} = \left(V + \frac{\Delta V}{2}\right) \cdot \Delta V \quad (27)$$

Equating the change in kinetic energy per unit mass to a change in potential energy

$$g \cdot \Delta h = \left(V + \frac{\Delta V}{2}\right) \cdot \Delta V \quad (28)$$

Solving for the change in "potential altitude"

$$\Delta h_{potential} = \left(V + \frac{\Delta V}{2}\right) \cdot \frac{\Delta V}{g} \quad (29)$$

The result in Eq. (29) demonstrates that the C-BAS system is most effective in changing potential altitude when initiated very early in flight. However, during the ballistic flight phase the vehicle is continually decelerating (due to the vehicle drag), and the C-BAS working fluid (CO_2) will be pinned against the front end of the tank. This event would result in only vapor leaving the exhaust port at the bottom end of the tank. The exiting vapor has the effect of rapidly cooling the tanks; causing reduced internal pressure, and eventually freezing the working fluid. To insure that only liquid and not vapor exits the tank, the C-BAS system is not activated until the vehicle drag, measured by the IMU's longitudinal acceleration, drops below the anticipated thrust level of the C-BAS exit steam.

B. Target Altitude Scheduling

The drag loss term in Eq. (3) is path dependent and is difficult to accurately calculate in flight with the C-BAS augmentation thrusters firing. The drag-loss parameter is best calculated pre-flight for a nominal trajectory and then used to schedule the "target altitude" as a function of the flight altitude. This approach allows the targeting algorithm to account for the anticipated drag-related energy loss along the flight path. The accumulated drag loss is added to the target altitude, nominally 1609.32 meters, to derive a target altitude schedule. Figure 15 shows the potential altitude loss due to drag along the flight path, and compares the target altitude to the potential altitude calculated using Eq. (26). The true altitude is also plotted for comparison purposes. The plotted data are results for a representative trajectory using approximately 2/3rd's of the total available C-BAS impulse and the assumed mean C-BAS thrust level is 10 Newtons. Pre-scheduling the target altitude improves the algorithm efficiency and has the effect of requiring less toggling of the C-BAS impulse to achieve the desired altitude. Pre-scheduling the target altitude results a nominal 10% cold-gas propellant savings.

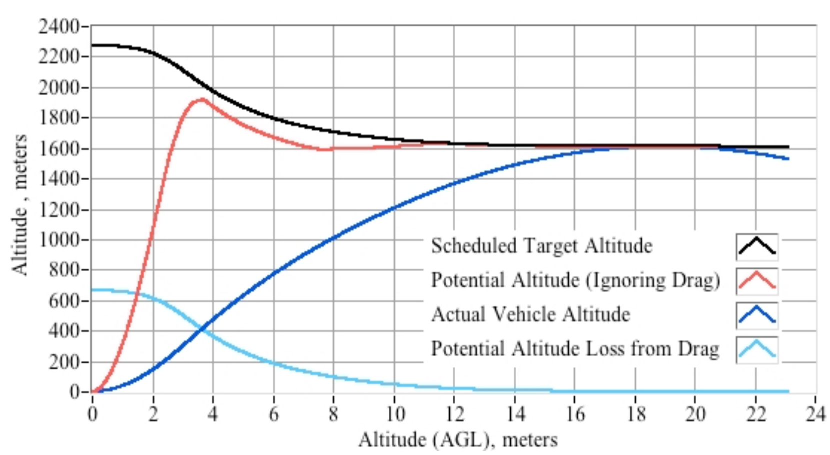

Figure 15. Potential Altitude Loss due to Drag and Target Altitude Schedule.

C. C-BAS Activation Control Law

A simple pulse-width modulation algorithm is used to control the vehicle energy levels. Following the motor burn out, the onboard flight computer continually calculates potential altitude, axial deceleration, and drag of the vehicle. Due to the CO_2 being in a saturated state, there will be two-phase flow as the fluid exits the tank. Drawing vapor from the tank significantly cools the tank, and the gas pressure being delivered to the aerospike plenum chamber drops dramatically. Insuring that the thrust from the spikes exceeds the drag of the vehicle before operation insures that the fluid leaving the tank exit is liquid. Once the calculated drag drops below the predicted nominal C-BAS thrust level, the energy management algorithm is activated. Figure 16 shows the energy management calculation sequence. Here h_{min} is the altitude at which the drag drops below the available thrust level, and h_{target} is the target apogee altitude.

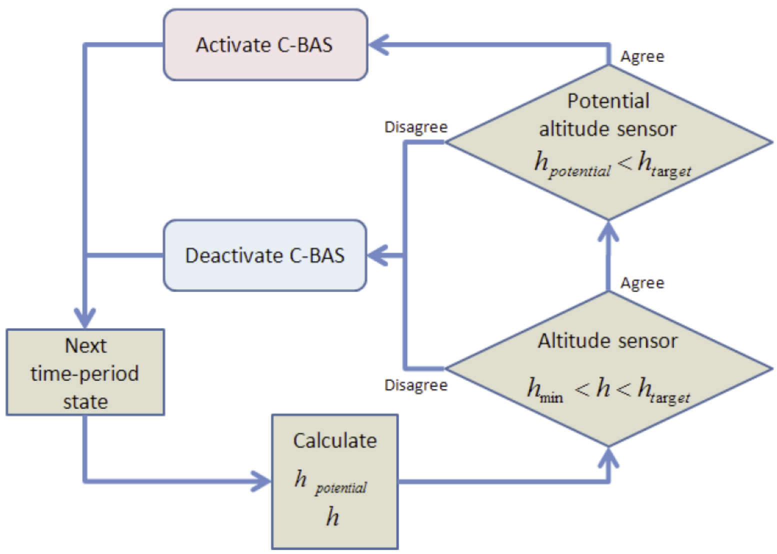

Figure 16. Energy Management Control Algorithm.

VII. Ground Test and Evaluation

Extensive preliminary ground tests were performed to demonstrate the functionality of the flight subsystems and to calculate or measure key vehicle performance parameters. This section presents results of the ground evaluations performed to estimate and verify the vehicle aerodynamics, main launch motor performance, and C-BAS thruster performance characteristics.

A. Vehicle Aerodynamics

Since the Javelin is designed to fly passively along a ballistic trajectory, detailed knowledge of the vehicle longitudinal centers of pressure and center of gravity during flight was essential to insure both static and dynamic stability. Accurate knowledge of the vehicle aerodynamic parameters including lift, pitching moment, and drag coefficient was essential to insure proper operation of the energy management system. Initial estimates of the vehicle lift, drag, and pitching moment coefficients were obtained using the Air Force missile flight dynamics code, Missile DATCOM. [21] The initial DATCOM drag coefficient estimates were corroborated using the commercial rocketry analysis code, AeroCFD[22], and a skin-friction/pressure correlation model developed by Drew and Jen.[23] Finally, wind tunnel wake surveys were performed using a 1/5th scale model to directly measure the vehicle drag coefficient. Center of pressure, static margin, and lift/pitching moment coefficients will be presented first. Discussions of the drag coefficient data will be deferred until after the wind tunnel wake survey test procedures and results are presented.

1. Static Stability

In the design phase, computer-aided design (CAD) models and mass-distribution spreadsheets were used to estimate the center of gravity (C_g) location. Once the vehicle was built these calculations were verified by direct measurements. Early center of pressure (C_p) estimates were derived using Barrowman's Method.[24] These C_p calculations were then verified using the Missile DATCOM, and AeroCFD. Finally, these results were experimentally verified through a series wind tunnel tests. The wind tunnel tests will be described later in this section. Figure 17 shows the calculated time-of-flight locations of C_g and C_p for the various computational models. The variation in static margin, defined by Eq. (30), is also plotted.

$$\chi_{sm} = \frac{x_{cg} - x_{cp}}{D_{body}}, \qquad (30)$$

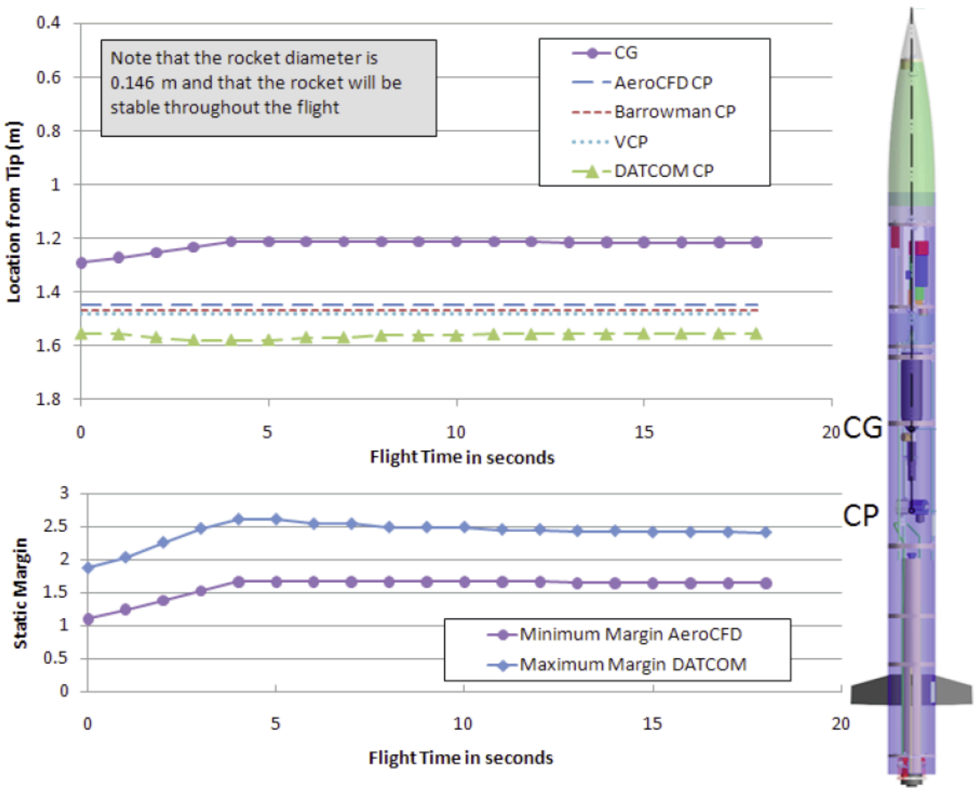

Figure 17. Time-of-Flight Center of Mass, Center of Pressure, and Static Margin Profiles.

A simple wind tunnel test was performed using a 1/5th scale model of the Javelin to verify the analytical static-stability calculations. Figure 18 shows the test setup. A rod was attached at the approximate center of gravity location allowing the model to pivot freely about that point. The attachment point was subsequently moved aft until the rocket no longer had a positive restoring moment. This neutral point was marked as the center of pressure. With the C_g behind the C_p, any disturbance caused the model to go unstable. Once the location of the center of pressure was determined, the rod was then moved back to actual scaled location of the Javelin's C_g. The model was placed at various trim angles and allowed to rotate freely. The stability was checked for predicted center of gravity locations at launch, motor burnout, and flight apogee. For angles less than 25 degrees the rocket returned and aligned with the airflow. Only minor overshoot was noted and the oscillation quickly damped. This result clearly indicates that the javelin airframe is both statically and dynamically stable for the ranges of C_g and C_p to be experienced in flight.

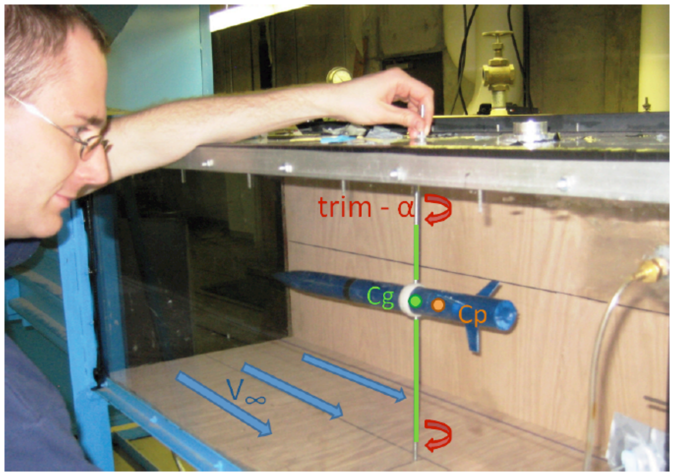

Figure 18; Setup for Wind Tunnel Tests Verifying Javelin Longitudinal Center-of-Pressure Location.

2. Lift and Pitching Moment Coefficients

Figure 19 presents Missile DATCOM-derived lift and pitching moment coefficients plotted as a function of angle of attack and Mach number. Since the expected maximum Mach number for the Javelin flight trajectory does not exceed Mach 0.5, only the low subsonic Mach numbers were investigated. As expected the lift coefficient shows an almost linear trend with angle of attack and only a minor effect due to compressibility. The pitching moment shows a slight non-linearity at angles beyond 5.0 degrees. The presented results are typical of a rocket with a high fineness ratio as is the Javelin.

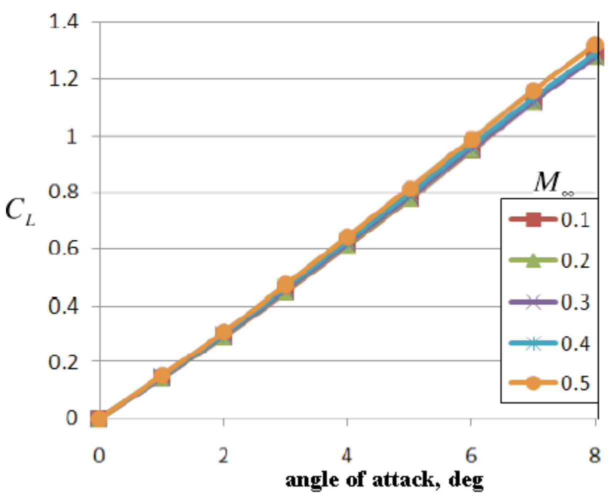

a) Lift Coefficient

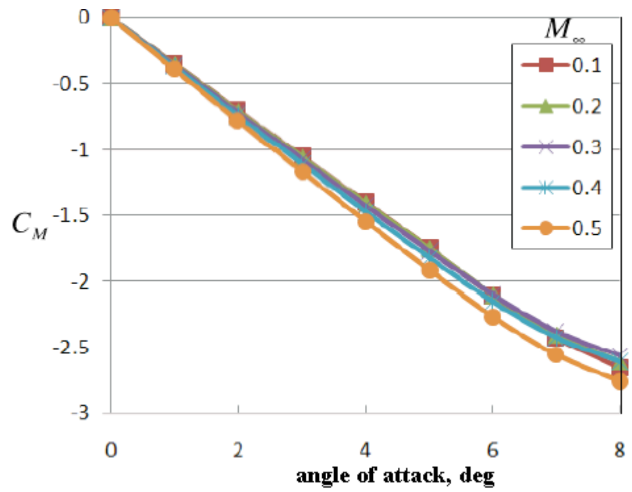

b) Pitching Moment Coefficient

Figure 19. Missile DATCOM Predictions of the Vehicle Lift and Pitching Moments.

3. Wind Tunnel Wake Surveys

This section describes the experimental apparatus and procedures, and presents test results from wind tunnel wake surveys performed to measure the 1/5th scale model drag coefficient. The Mechanical and Aerospace Engineering department at USU has at its disposal a small subsonic wind tunnel with an approximately *30 x 30 cm* wide by *100 cm* long test section. The empty wind tunnel can reach speeds of approximately 30 m/sec (*98 ft/sec*). This airspeed produces a dynamic pressure of approximately *0.48 kPa (10 lbf/ft^2)*. Because of the low dynamic pressure levels and small test section size, wake survey methods were considered to be far more accurate for measuring the drag coefficient than direct load measurements using a support sting and force balance. Also, due to the potential for wall reflections and tunnel flow blockage at high angles of attack, only low angle of attack measurements are considered valid. Although the maximum tunnel speed is significantly lower than the maximum speeds reached by the rocket in flight; the wake survey methods nonetheless provide a good measure of the incompressible drag coefficient and results in a good "sanity check" on the analytical calculations.

For the wake surveys, the model was mounted on a moveable support rod, and a traversing pitot/static probe was mounted on a traversing rack and pinion drive. A small electrical motor drives the traversing mechanism, and the probe position is sensed by a small linear potentiometer. A high-resolution MKS® 223BD differential manometer sensed the differential pressure across the probe. Omegadyne® 142PC15A 0-15 psia (103 kPa) absolute Omegadyne®143PC01D $\pm$1 psid ($\pm$6.9 kpa) differential pressure transducers sensed the tunnel reference total and static pressure values ahead of the model, respectively. An additional Omegadyne® 143PC01D $\pm$1 psid differential pressure transducer sensed the wall static pressure at the pitot probe location. A 12-bit National Instruments PCMCIA data acquisition card sampled the measured data. Results were logged on a laptop computer running Labview 10®. **Figure 20** shows the model mounted in the tunnel, along with the pitot traversing probe, and the instrumentation suite. The backside tunnel wall has been removed to allow greater visibility for this picture. **Figure 21** shows the instrumentation layout and wiring diagram for the wake survey tests.

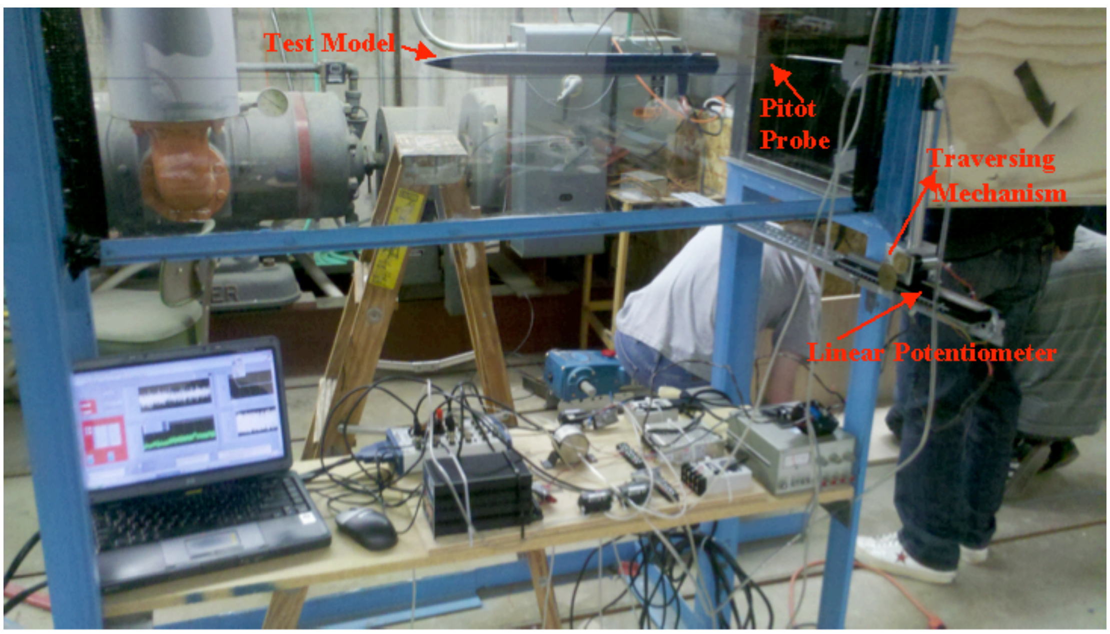

Figure 20. 15th Scale Model Model and Pitot Tube Inside Wind Tunnel.

The support rod allowed the model to be positioned at a variety of vertical settings, and at each setting the probe was swept across the wake recording local differential pressure (proportional to airspeed). The linear potentiometer senses the horizontal probe position, and allows a nearly continuous horizontal pressure distribution to be measured. For each complete survey a total of 8 evenly spaced horizontal sweeps were obtained for vertical locations from *60 mm* above to *60 mm* below the center waterline of the model. Complete wake surveys were obtained with the tunnel speed setting at 50%, and 100% power level. Multiple wake surveys were obtained for these tunnel speed settings to allow ensemble set averaging and noise filtering to be performed.

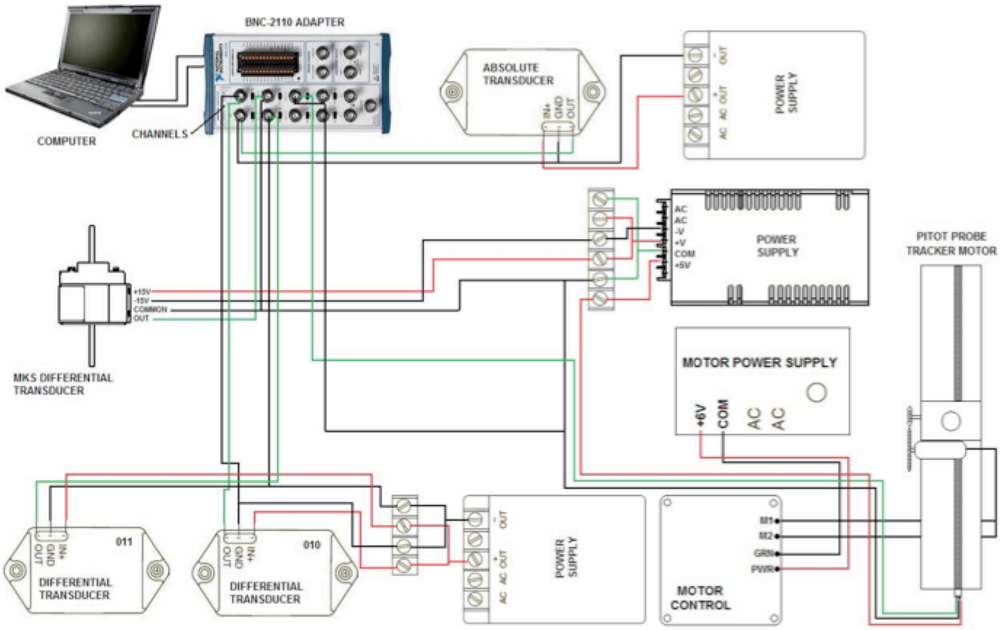

Figure 21. Wind Tunnel Test Instrumentation Layout and Wiring Diagram.

Following the method developed by Whitmore, Sprague, and Naughton,[25] the drag coefficient can be expressed as a polar area integral of the total momentum defect in the wake

$$C_D = \frac{8}{\pi \cdot D_{body}^2} \int_0^{2\pi} \left[\int_0^{\delta_{wake}} \left(\frac{u}{V}\right)_{r,\varsigma} \cdot \left(1 - \left(\frac{u}{V}\right)_{r,\varsigma}\right) \cdot r \cdot dr \right] \cdot d\varsigma \quad . \tag{31}$$

In Eq. (33) the parameter $(u/V)_{r,\zeta}$ is the local normalized velocity defect. The local velocity defect is calculated by interpolating the wake survey velocity defect data at the proper coordinate location (r,ζ) in the flow field. The radial and polar coordinates are calculated from the local lateral and vertical coordinates by

$$r = \sqrt{x^2 + y^2}$$
$$\varsigma = \cos^{-1}\left(\frac{y}{x}\right) \tag{32}$$

The local velocity defect is calculated from the pitot/static pressure data assuming incompressible flow and no tunnel stagnation pressure loss from the reference port to the probe station

$$\frac{u}{V}_{(y,z)} = \sqrt{\frac{\frac{2}{\rho}\left(P_0 - p\right)_{(y,z)}}{\frac{2}{\rho}\left(P_0 - p\right)_{edge}}} = \sqrt{\frac{\Delta p_{(y,y)}}{\left(P_0 - p\right)_{edge}}} \quad . \tag{33}$$

The coordinates (x,y) represent the local vertical and horizontal position of the probe tip. The probe tip was axially positioned approximately 4 cm behind the model. The term $(P_0-p)_{edge}$ is the difference between the reference tunnel pitot pressure and the wall static pressure at the probe survey station.

Figure 22 shows the filtered and processed results of a typical wake survey. Here the normalized velocity defect u/V is plotted as a function of the vertical (z), and lateral horizontal (y) position behind the model. Axial, top, and isometric views of the wake survey data are presented. Several features are clearly visible including the three model fins and the base wake. The data show very good axial symmetry indicating that a zero angle of attack condition was measured.

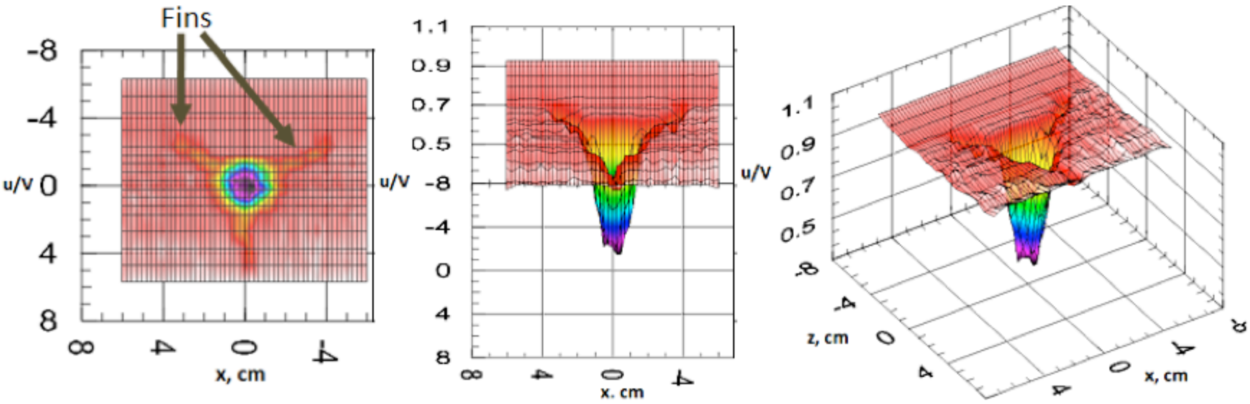

Figure 22. Typical Survey Results Showing Velocity Defect in Model Wake.

4. Drag Coefficient Comparisons

Figure 23 compares the drag coefficients obtained from the previously described analytical methods and the wind tunnel wake surveys. Here the wake survey C_{D0} has been adjusted for compressibility using the Prandtl-Glauert[26] subsonic correction for comparison with the other models. Not surprisingly the wind tunnel data show the highest drag coefficient. This result is likely due to Reynold's number scaling and surface roughness effects. Based on this ensemble of data, the mean C_{D0} is approximately *0.365* with a standard deviation of ± 0.17 (95% confidence level based on 5 ensemble members).

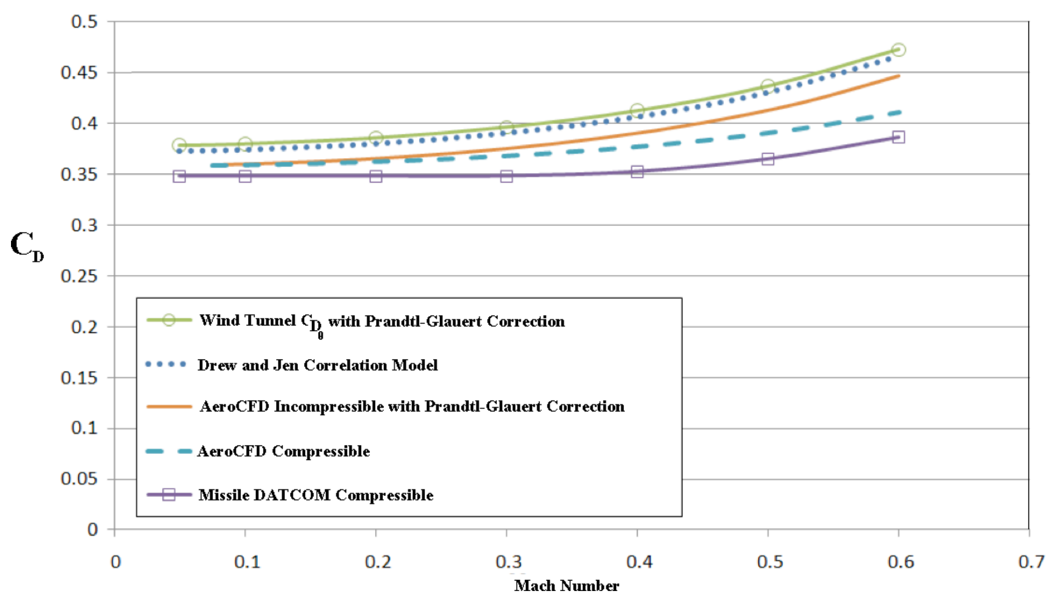

Figure 23. Drag Coefficient Comparisons for Various Analytical and Experimental Sources.

C. Main Motor (Cesaroni L-730) Thrust Measurements

As presented earlier in the *Systems Engineering* section, the manufacturer's specifications for the Ceraroni L-730 predict a mean thrust level of *730 N*, a burn time of *3.8 seconds*, and a total impulse of *2765 N-s*. Early flight simulations showed that these motor capabilities achieve the mission objectives. However, because of the well known potential for large motor thrust and total impulse variations, it was imperative for the Chimaera team to procure and test multiple motor reloads to establish the true mean motor parameters and accompanying uncertainties. Test data gathered from three independent motor burns was compared to existing published data for the L-730 motor.

An existing 6-degree of freedom static test at Utah State University was used to perform the motor tests. Only the axial (thrust), and vertical (weight) load measurements were used for these tests. The thermocouples mounted on the external motor case measured the temperature during and after the burn. This temperature measurement was required to insure that the motor case did not exceed operating limits for the flight hardware. Because the USLI rules precluded modifications of the stock motor, chamber pressure was measured for the initial thrust stand shakedown tests, but was not measured for the L-730 characterization tests The chamber pressure measurements required modifying the motor cap with a threaded access port. The axial load was sensed by an Omegadyne® LCCB-500 2225 N (500 lbf) load cell. Vertical loads were sensed by two Omegadyne® LC101-25 112 N (25 LBF) Load Cells. Both load cell types provided 3mV/Volt output. Type-K thermocouples were used for the case temperature measurement. Data acquisition was performed using the 16-bit National Instruments Compact-DAQ® Universal Serial Bus (USB) data acquisition system. Data were monitored and logged using a test laptop running Labview® 10. The test laptop resided within the test cell. A remote laptop, located in the control room, was used to log into the test laptop via Ethernet and a remote desktop application. Remote access was a safety to protect the test team in the event of a motor explosion. Figure 24 shows the thrust-stand instrumentation system and an image of a candidate rocket motor being tested. The motor was ignited using the normal flight launch controller (Figure 9).

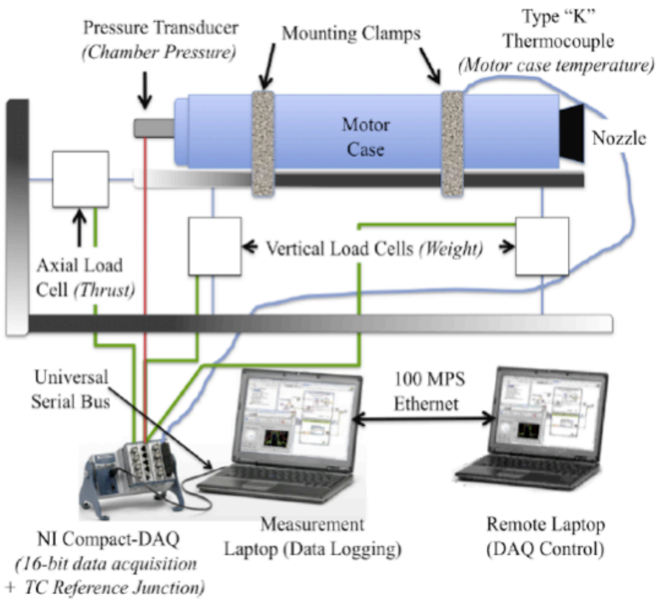

a) Static Thrust Stand Instrumentation Schematic

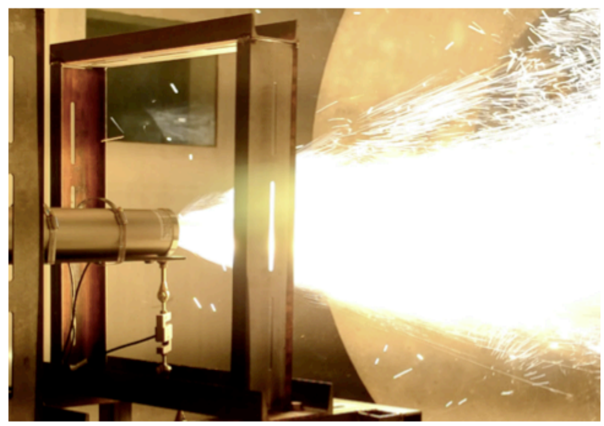

b) Image of Test Motor Firing

Figure 24. Rocket Static Thrust Test Stand.

Figure 25 shows the characterization test results where the thrust and impulse burn-time profiles are compared against existing thrust and impulse curves obtained from Ref. 5 and from the manufacturer.[27] All thrust and impulse profiles have been corrected to sea level standard conditions. The thrust profiles show a wide variability in peak thrust and curve shapes; however, the total impulse curves are reasonably consistent. Interestingly, the one motor test that exhibited the lowest peak thrust level, also had the highest overall impulse level. This outlier test was conducted on a particularly cold day (the test cell is open to ambient conditions), and grain temperature is the likely source of this variability. The mean total impulse is *2779 N-s (624.90 lbf-s),* with a standard deviation of *±47.25 N-s (±10.62 lbf-s).* With 4 degrees of freedom (5 data sets), the 95 percent confidence uncertainty of the total impulse is *±131.28 N-s* (*±29.51 lbf-s*). The 95% confidence interval variation of total impulse is *±4.7* percent, significantly less than the 20% motor-to-motor variability that was expected. Thus, the L-730 motor reloads were verified as completely acceptable to meet the program requirements.

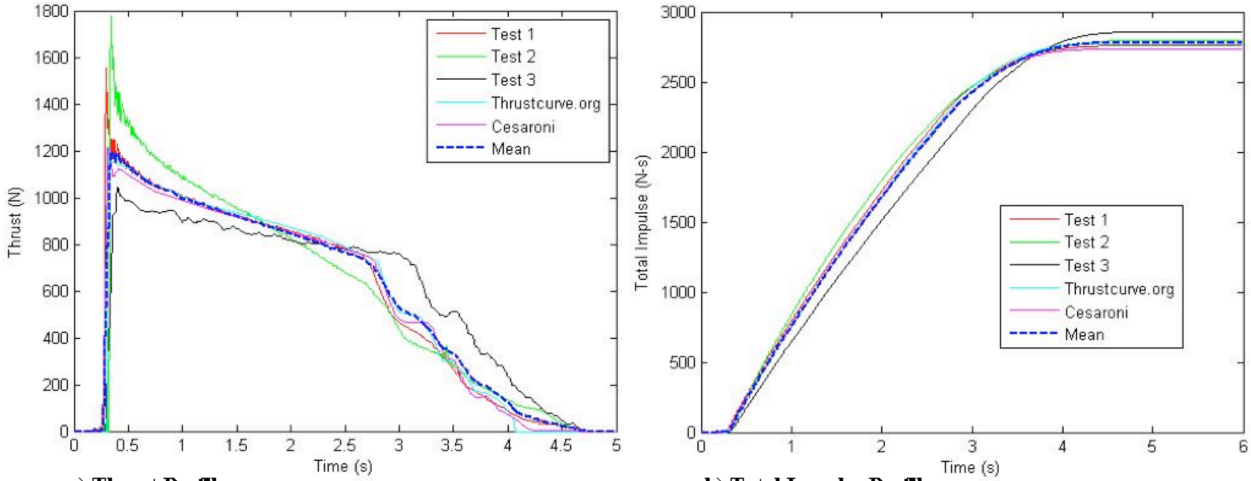

a) Thrust Profile **b) Total Impulse Profile**

Figure 25. Thrust and Impulse Burn-Time Profiles for Cesaroni L-730 Motor.

The final L-730 characterization test was performed with the motor mounted in the airframe tube along with the C-BAS CO_2 tank and associated pneumatic hardware. Thermocouples were mounted on the motor case near the nozzle, near the forward end of the motor case, and on the CO_2 tank. A secondary objective of this final test was to verify that the motor soak back would be insufficient to raise the CO_2 tank temperature to a critical level where an explosion or burst disk rupture could occur. Figure 26 shows the recorded temperatures from this test. Even though heat soak back causes an aft motor case temperature rise to 135 C approximately 75 seconds after motor burnout, the CO_2 tank temperature does not measurably rise from the ambient temperature level. This result confirms that post flight motor heat soak back does not present a flight or ground crew safety issue.

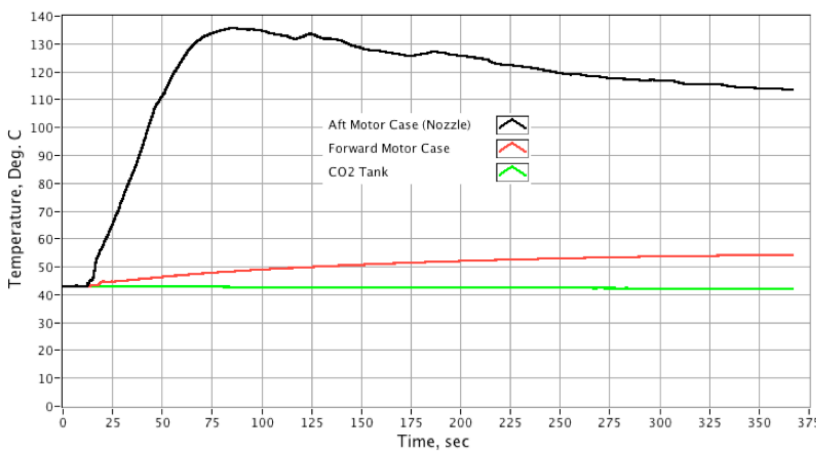

Figure 26. Cesaroni L-730 Motor Static Test #3 Temperature Profiles.

C. C-BAS Thrust and Impulse Characterization Tests

C-BAS characterization ground tests were performed using a custom designed test stand. Figure 27 shows a schematic of the test apparatus, and an image of the thrusters "firing". Axial loads were measured using an Omegadyne® LC101-25 112 N (25 LBF) Load Cell and the regulator output pressure was sensed measured using an Omegadyne® PX139 3450 kPa (500 psia) absolute pressure transducer. A type-K thermocouple was mounted to the regulator outlet to monitor temperature. The C-BAS port side ramp pressures were measured using the flight transducers described earlier in the *Payload Overview* section. A National Instruments NI-6009® 14-bit USB Data acquisition device was used to sample the data. The solenoid valve was controlled using a National Instruments USB-9472 digital relay device. Data were monitored and logged using a test laptop running Labview® 10.

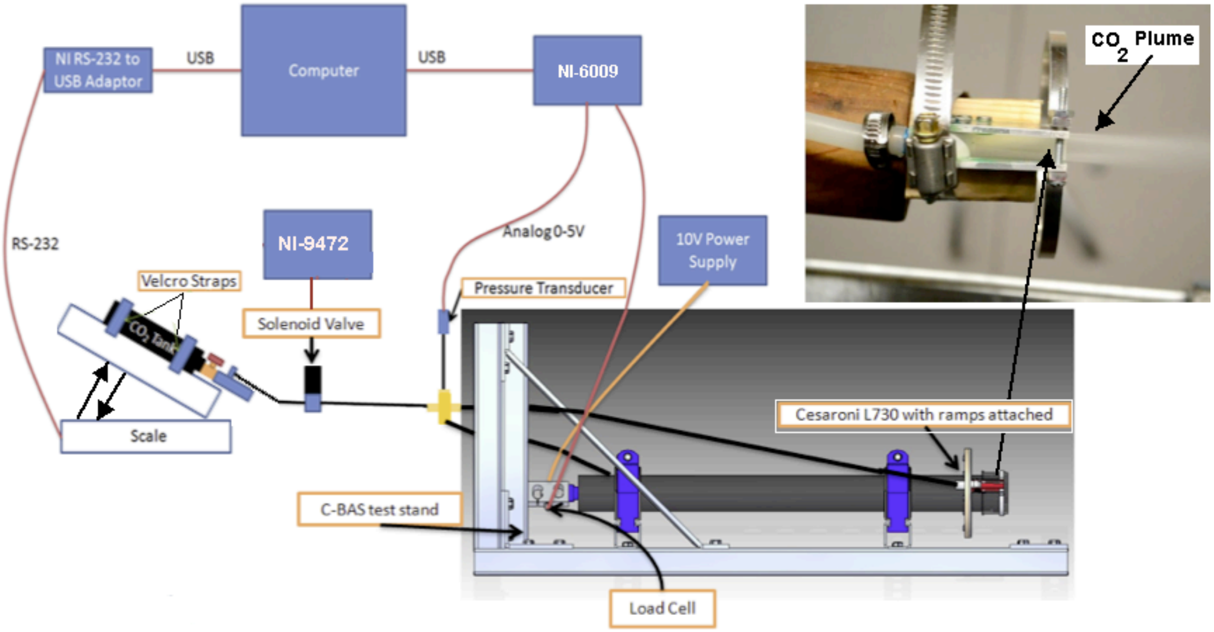

Figure 27. C-BAS Static Thrust Test Stand.

During initial C-BAS tests, the system was checked for leaks by spraying a bubble-forming high-visibility leak detector around all major component junctions. Regions that showed evidence of leaking were reinforced with a silicone sealant with a temperature range sufficient for all aspects of the rocket flight environment. Line losses downstream of the regulator outlet were small enough that the sensed pressure was assumed to be identical to the actual aerospike thruster plenum pressure. Rubber support bands were used to constrain the empty test motor with aerospike thrusters attached. These support bands allowed complete transmission of axial forces but constrained lateral movements. The CO_2 tank was elevated at a 45-degree angle to insure that only liquid propellant leaves the tank. The tank weight was monitored during the test using a commercial parcel scale with a serial output. Figure 28 shows the locations of the surface ramp ports along the spike contour.

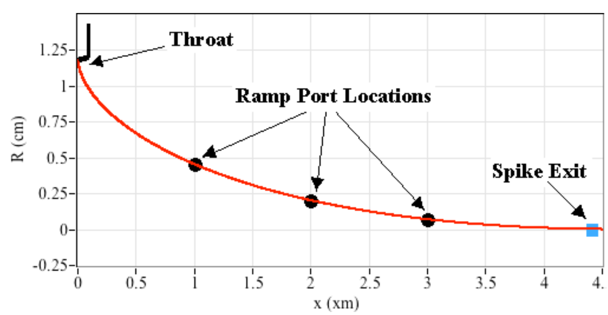

Figure 28. Ramp Pressure Port Locations Along Aerospike Contour.

Figure 29 shows representative test results from a ground test where the solenoid was pulsed in two-second intervals with a 50% duty cycle to emulate the on-off flight operation of the C-BAS. A 20 second duration test was performed to approximate the anticipated time-of-flight to apogee for the vehicle. Figure 29a plots the outlet pressure time history, Figure 29b plots the thrust, and Figs. Figure 29c, d, and e plot the surface ramp pressures. Figure 29f plots the total accumulated impulse. The black lines on the graphs show the measured data; the red lines on plots b-f show the analytical calculations assuming the plenum pressure is the same as the measured outlet pressure.

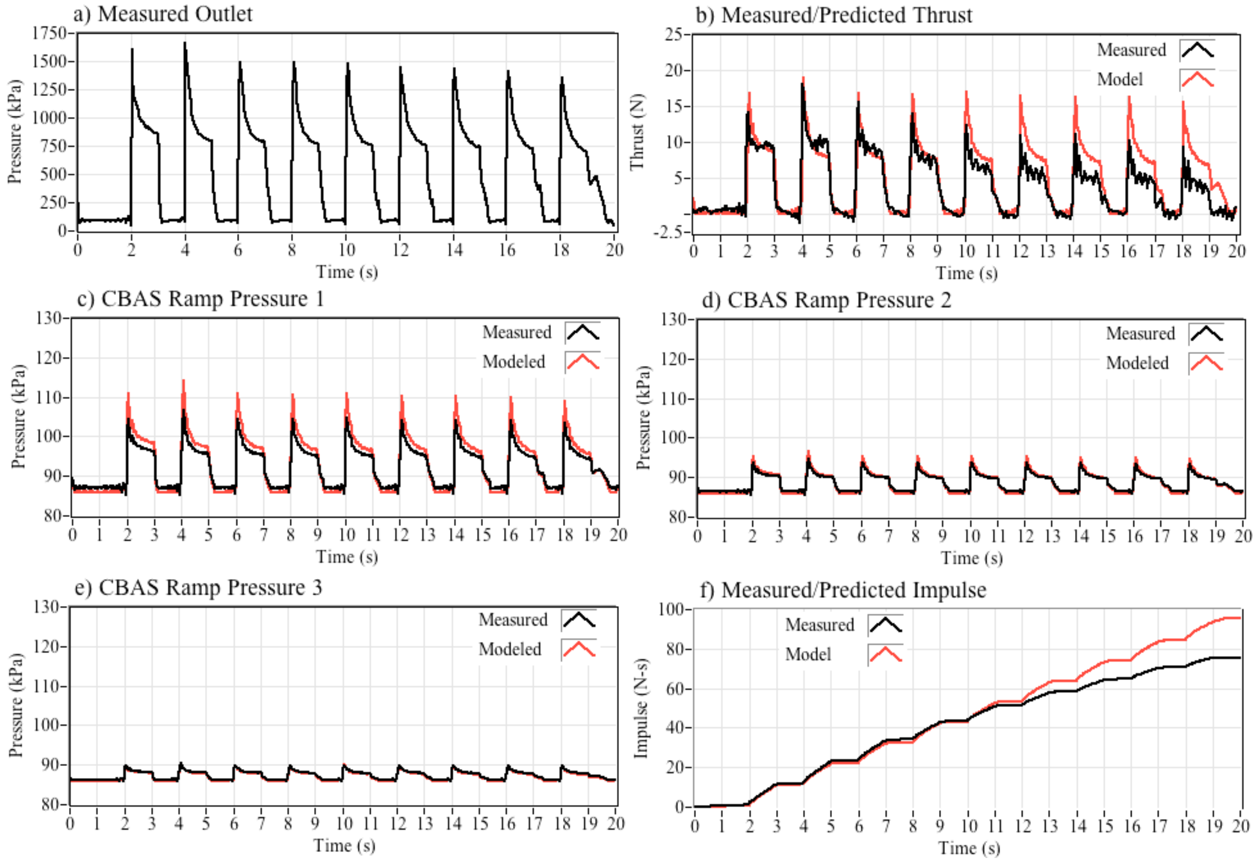

Figure 29. Representative C-BAS Ground Test Results.

The measured regulator pressure is not constant for the pressure pulses; but instead peaks sharply, and then decays over the course of the pulse following a first-order decay pattern. This pattern is an artifact of the regulator dynamics, and could not be modified for the current design. A slight drop in the measured outlet pressure for successive pulses can also be seen in these graphs. The resulting thrust pulses exhibit a similar "peaked" shape. Interestingly, while the outlet pressure remains relatively constant for each of the solenoid pulses, the thrust levels continually drop. Comparing the predicted thrust levels, which assume adiabatic flow, the thrust drop indicates that the system is getting continually colder as the liquid CO_2 flashes to vapor and expands. As the thrusters cool, the plenum pressure drops and the thrust level drops proportionately. This total impulse comparison also clearly supports the "cooling" hypothesis. The predicted total impulse for the 20-second test is approximately 95.8 N-s, the measured impulse is 75.6 N-s, and represents a loss of approximately 23%. Fortunately, the majority of the impulse loss occurs after 15 seconds of pulsed operation. For flight conditions, after fifteen seconds following main motor burnout the vehicle is near apogee. Thrust and impulse levels required to trim the vehicle are low near apogee.

VIII. Flight Tests

A total of three Javelin test flights were performed during the 2010-2011 academic year; two qualification flights in preparation for the USLI competition, and the final competition flight. For the team to qualify to participate in the USLI competition, at least one successful launch and recovery prior to the USLI-mandated flight readiness review (FRR) was required The compressed time scale of the USLI competition schedule allow very little time for the flight teams to "wring out" their flight systems through a conservative envelope expansion process. Thus the qualification tests flights often involve an "all or nothing" mentality. As will be described in the next section, this approach very nearly cost the USU Chimaera design-team it's slot in the USLI competition.

A. Preliminary Flight Test Results

The first test flight of the Javelin occurred on March 19, 2011 at the Pony Express Test Range outside of Lehi, Utah. Conditions at the site were less than ideal. Sustained winds of 20 kts and gusts exceeding kts mph made launch preparations a challenge. The first test flight attempted to fly all of the vehicle subsystems, and had a successful launch but a recovery system failure. The failure resulted in a hard landing and the vehicle sustained significant damage. Fortunately, many of the vehicle sub systems remained intact including most of the avionics. Unfortunately, the hard impact damaged the IMU and detailed trajectory information was not obtained from that flight. A backup engineering development unit (EDU) was used to replace the damaged unit for the USLI competition fight. Figure 30 shows the vehicle at launch and after the unsuccessful recovery.

Figure 30. Javelin Flight 1, Launch and Unsuccessful Recovery.

To determine the cause for the accident, Chimaera project members and the USU faculty formed a post flight accident investigation board. A key fact in the accident investigation was that none of the 4 recovery system ejection charges had burned, indicating a single point failure with power distribution to electronic matches. The investigation board ultimately determined that both altimeters had been incorrectly hard-wired in "communication mode." In this mode the altimeters were expecting commands from a controlling laptop to dump stored onboard data. Wired in this manner the altimeters never sensed the launch, apogee, or main parachute deployment altitude events. Also, because of this error, neither altimeter recorded the flight trajectory data. The wiring was corrected, and mitigation procedures were established to verify on the launch pad that the altimeters were properly configured, and properly sensed the launch, apogee and chute deployment events. Finally, several heavy flight components including the C-BAS solenoid valve were swapped with lighter weight components, and approximately 0.75 kg of mass was shed from the launch weight. The airframe was subsequently rebuilt and a second test flight was performed.

The second flight occurred on March 26, 2011 at the Pony Express test range. The primary objective of this second flight was to successfully launch and recover the vehicle. Collecting a minimal set of trajectory data to verify the successful flight was an important secondary objective. To simplify operations the vehicle was not fully instrumented with the full avionics suite. Instead only the two PerfectFlite altimeters, the recovery systems components, and power distribution boards were flown. A separate R-DAS system was flown to log the vehicle acceleration and altitude. The IMU, Gumstix flight computer, and telemetry systems were not flown. The C-BAS hardware was flown, but was not activated during flight.

The Javelin was successfully launched and recovered. Salvaging, rebuilding, and flight testing a rocket of this complexity in a single week was a remarkable achievement for the Chimaera team. Again, for this flight the weather conditions were less than ideal with 20-25 knot winds and very cold conditions. For flight 2 the vehicle only achieved an apogee altitude of 1000 meters above ground level. Data presented in Figure 31 explain the reason for this low flight apogee. Figure 31 plots the flight 2 launch trajectory derived from the primary perfect flight altimeter and the R-DAS-measured accelerometer and altitude data. Because they are derived by numerically differentiating the accelerometer data, the vertical velocity and flight path angle are rather noisy. In spite of the noise, the flight path angle data show that the initial launch angle was significantly off from vertical – as much as 20 degrees. When this 70-degree initial launch pitch launch angle is input to the simulation using the actual vehicle launch mass (12.59 kg) , the mean motor thrust curves (Figure 25), and the best known mean drag coefficient ($C_{D0}=0.365$); the measured flight trajectory is closely reproduced.

During pre-launch preparations the launch pad team noted that the vehicle was significantly harder than normal to slide onto the launch rail. Thus, it appears that the blustery conditions blew up considerable sand and silt which partially clogged the slots on the launch rail. During launch the rail lugs partially bound up causing the vehicle to depart at a lower than planned rail velocity. This low launch velocity coupled with the high cross winds caused the vehicle to pitch by approximately 20 degrees as it departed the rail. Simulation calculations show that the vehicle went through apogee with a horizontal velocity exceeding *70 m/sec*. Much of the potential altitude was wasted as unnecessary horizontal velocity. Fortunately, L-730 motor appeared to have burned nominally, and the simulation comparisons verify that the preflight prediction for drag coefficient is close to what was actually achieved.

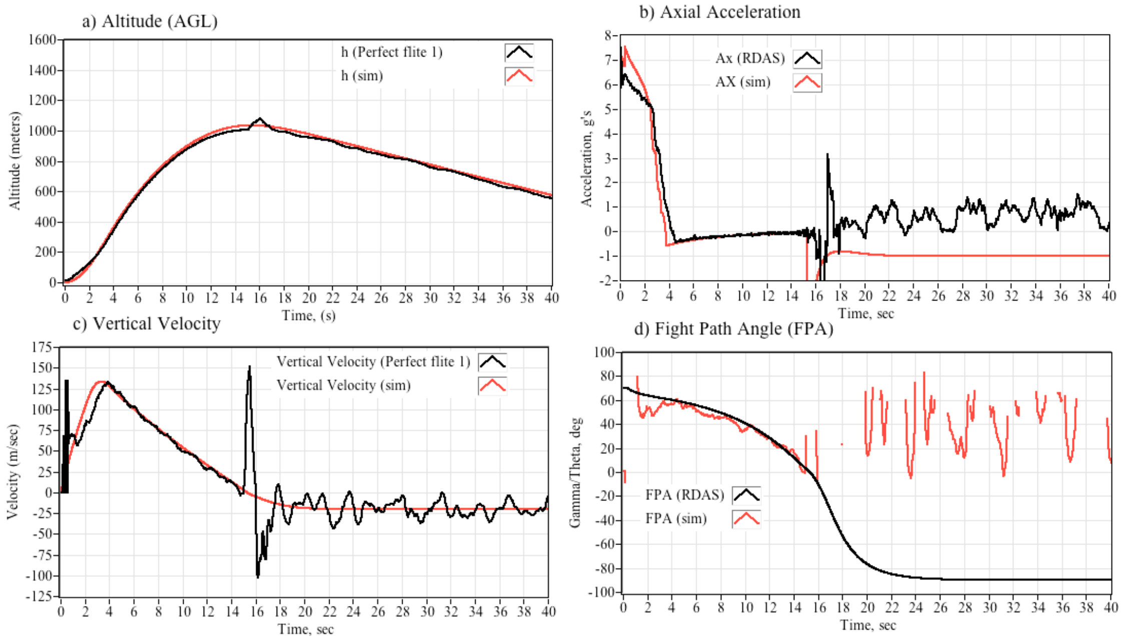

Figure 31. Flight 2 Trajectory Reconstructed from PerfectFlite, R-DAS Data.

Based upon this analysis, and the successful launch and recovery, the Chimaera team felt confident to press forward with the competition launch. Several minor changes were made to the vehicle to gain a higher launch "ΔV." The launch rail was scrubbed, polished, and dry-lubricated to make it significantly "slicker." To prevent binding original plastic launch lugs were replaced with aluminum lugs. The very rough surface coat of the second launch airframe was made significantly less "draggy" by better sealing on the avionics and C-BAS bay access doors, painting and sanding the airframe surface, and applying a plastic MonoKote® film to the airframe.

B. Competition Flight Test Results

The 2011 USLI launch competition was held on April 17, 2011 at the Bragg Farms launch site in Toney Alabama. A total of 29 university teams were entered into the competition, but technical difficulties kept several of the teams from actually launching. According to the competition PerfectFlite altimeter, the Javelin achieved an altitude of 1665 meters (5465 ft) above the launch ground level. Of all the teams entered into the USLI competition, this altitude was the 7th closest overall The competition altimeter varied slightly from the back-up recovery system altimeter, which read 1659 meters (5443 ft). The discrepancy shows the lack of fidelity in low-end hobby rocketry components. Figure 32 shows the altitude time histories retrieved from both PerfectFlite. The data was filtered to eliminate the apogee altitude spike. The apogee spike is likely caused by the ejection charges creating a vacuum in the avionics bay, with the resulting low pressure causing the altimeters to register a sudden increase in sensed altitude.

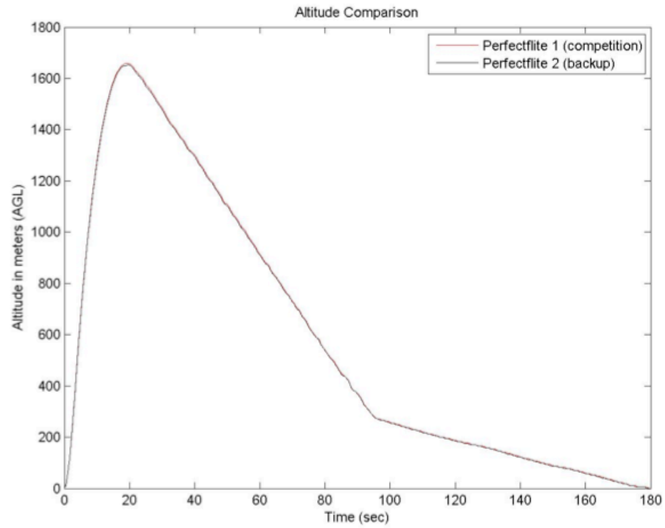

Figure 32. Time-of-Flight Altitude Comparisons of the Competition and the Back-up Altimeters.

There are several factors that could have produced the higher than anticipated apogee altitude (3.5% error). Clearly, a less than vertical initial launch angle would produce a lowered apogee and is not a possible cause. The Chimaera team identified 5 most likely causes for the higher apogee; these are 1) lower than expected vehicle launch weight, 2) in-flight thermals and updrafts, 3) an anomalously large C-BAS total impulse, 4) an anomalously large L-370 motor burn impulse, and 5) lower than expected in-fight vehicle drag. Comparing the measured pre-and post launch weights with the expected values quickly eliminated items 1 and 3 in this list. The recorded pre flight weights agreed with the expected weight by less than 10 grams. Also, the post flight CO_2 tank weight indicated that no propellant was consumed; the C-BAS system did not operate. Similarly, Item 2 in the list was also quickly eliminated. The launch day was cool and stable with clear skies. A check of local national weather service records indicated a building area of high-pressure into the region. This synoptic pattern makes substantial thermal activity very unlikely. Thus by the process of elimination, only the anomalously high L-730 burn impulse, and reduced drag hypotheses remained as likely explanations. These two factors will be investigated in the following subsections.

1. Cesaroni L-730 Motor Flight Burn Profile

Figure 33 compares longitudinal acceleration during the climb to apogee and accumulated "ΔV" in *g-s* (the integral of the longitudinal acceleration) as measured by the IMU against simulation calculations perform using the best estimates of vehicle launch mass (*12.59 kg*) and drag coefficient ($C_{D0} = 0.365$). Since the post flight inspections verified that the C-BAS did not operate in flight, the simulation calculations assume no energy augmentation. Clearly, of flight while the motor is burning during the initial stages the acceleration and ΔV traces are nearly identical. Clearly, there is nothing anomalous about the burn profile of the L-730 motor. However, just before motor burnout, the flight data shows a slightly greater acceleration level, and the ΔV curves begin to diverge.

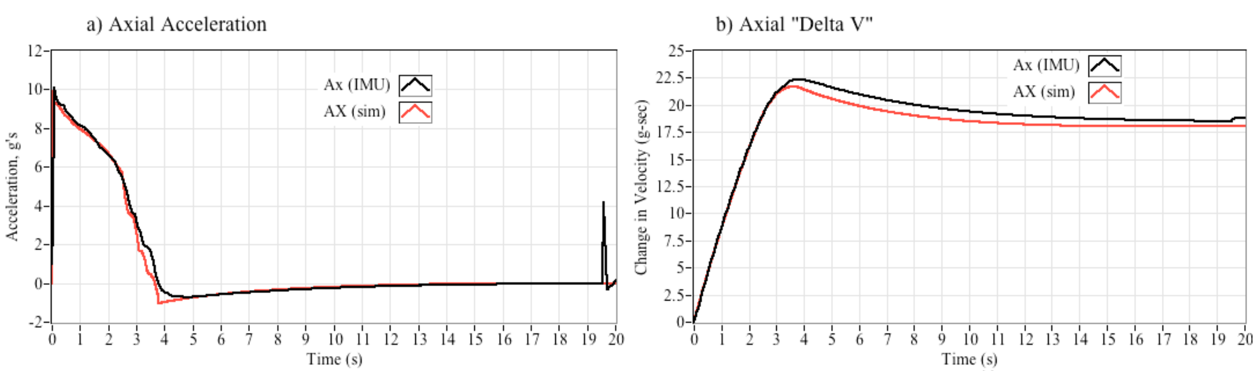

Figure 33. Competition Flight Axial Acceleration and ΔV Compared to Simulation with $C_{D0} = 0.365$.

When the simulation is re-run, but with a 25% lower drag coefficient ($C_{D0} = 0.285$), the flight and simulation time history traces are nearly identical. Figure 34 shows this comparison. These comparisons support the conclusion that the vehicle clearly experienced a lower drag-level in the competition flight than was predicted by the analytical models, wind tunnel tests, and the flight 2 trajectory data.

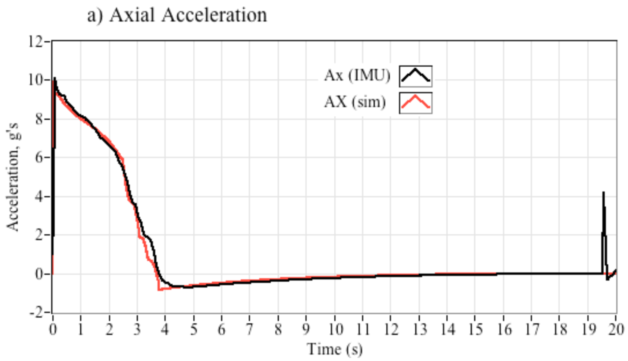

Figure 34. Competition Flight Axial Acceleration and ΔV Compared to Simulation with $C_{D0} = 0.285$.

2. Effect of Lowered Drag Coefficient

Figure 35 presents additional data to support this "reduced drag" hypothesis. The first graph 35(a) compares the altitudes and potential altitudes calculated from the competition Perfectflite altimeter and the IMU/Kalman filter with the simulation results assuming $C_{D0} = 0.365$. The second graph 35(b) repeats the comparison with $C_{D0} = 0.285$. In the first graph, the simulation predicts an apogee altitude of 1546.91 meters. In the second graph the simulation predicts an apogee altitude of 1663.03 meters, a value almost identical to the measured Kalman filter apogee, 1664.1 meters. No energy augmentation is active for any of the time history traces.

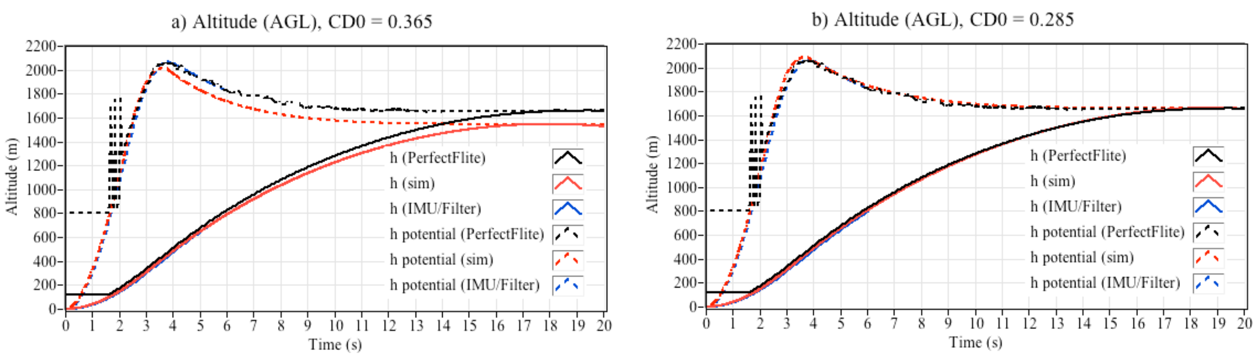

Figure 35. Altitude and Potential Altitude Comparisons for Nominal and Reduced Drag Profiles.

Because of the reduced drag, it is very likely that the energy bleed off during the ballistic phase of flight was lower than anticipated, and the overall energy level never crossed over the scheduled value for triggering C-BAS activation. Figure 36 illustrates this concept. Here the measured and predicted achieved altitude and potential altitude are compared against the C-BAS target altitude schedule. Following the main motor burnout at 3.8 seconds, the target schedule always remains below the calculated potential altitude trace. As a result, the C-BAS activation algorithm (Figure 16) never detected an "energy-low" event, and the energy management system was never operated.

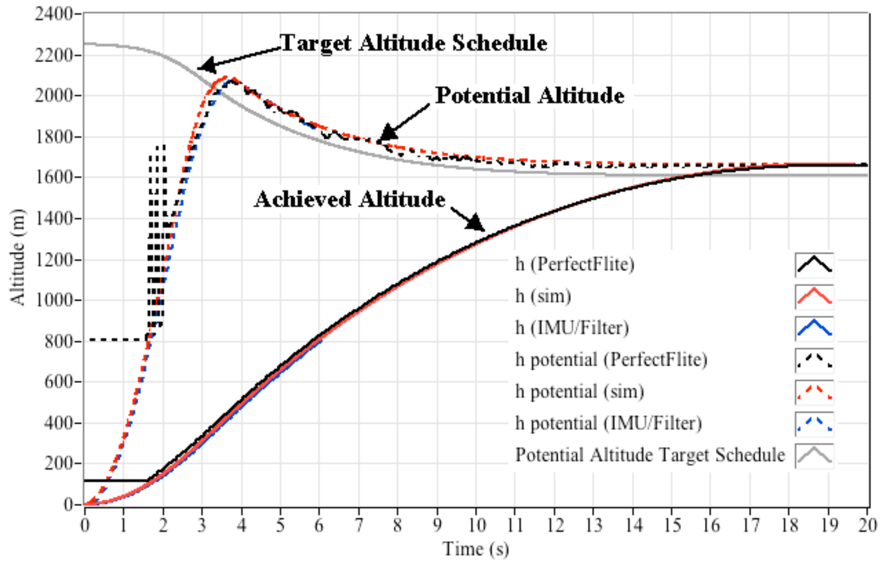

Figure 36. Comparison of Achieved and Potential Altitude to Target Altitude Schedule, C_{D0}=0.285.

2. Potential Reasons for the Reduced Competition Flight Drag Coefficient.

Reasons for the drag reduction from flight 2 to flight 3 are unclear; however, a significant reduction in skin friction is a likely cause. For the qualifying flight the vehicle was unfinished, and the airframe had a relatively rough sanded epoxy surface with gaps for the access doors. This rough surface likely tripped the flow and resulted in forced bypass turbulence very far forward along the body contour. Three changes implemented for the competition flight may have reduced this bypass transition effect. In preparation for the competition flight the Javelin was covered in hi-gloss MonoKote® over the majority of the exposed surface area, and a high-gloss paint was applied to the nosecone. Additionally 3.5 cm of length were removed from the center of the rocket to adjust the center of gravity. This reduction in the length of the rocket gave a lower Reynold's number and lessened the surface area that was exposed to turbulent flow. Finally, tape was added to secure the access doors. Rather than the gaps that were present on the flight 2 configuration, the tape created a continuous surface further removing turbulent triggers from the rocket. These three feature changes may have allowed a significant extension of laminar flow on the body. Extended laminar flow, if it occurred, would have produced a significant overall drag reduction.

3. CFD Solutions

To investigate this premise, a computational fluid dynamics (CFD) analysis was performed to examine the effects laminar and turbulent drag on the Javelin. A control volume of the subtracted model of the rocket was created using Solid Edge® computer aided design (CAD) software,[28] and a computational mesh was created using Gambit®.[29] The computational solver used the commercially available CFD code Fluent®.[30] Because the rocket can be considered periodic, the model and the control volume were cut in three sections to reduce the computational time. A triangular grid was chosen for the surface of the rocket and the interval size of the body was set to 10 units. The fin mesh was then refined to an interval size of 1 unit. Tetrahedral elements were used at an interval size of 100 units in the control volume. Figure 37 shows the meshing of the fins and body tube. The boundary condition for the upper surface of the control volume was prescribed as a solid boundary to further speed convergence time. Because the distance from the wall to the surface of the rocket is substantially large, this boundary condition did not affect the solution. The Fluent® model has 523,980 cells, 1,092,745 faces, and 110,424 nodes.

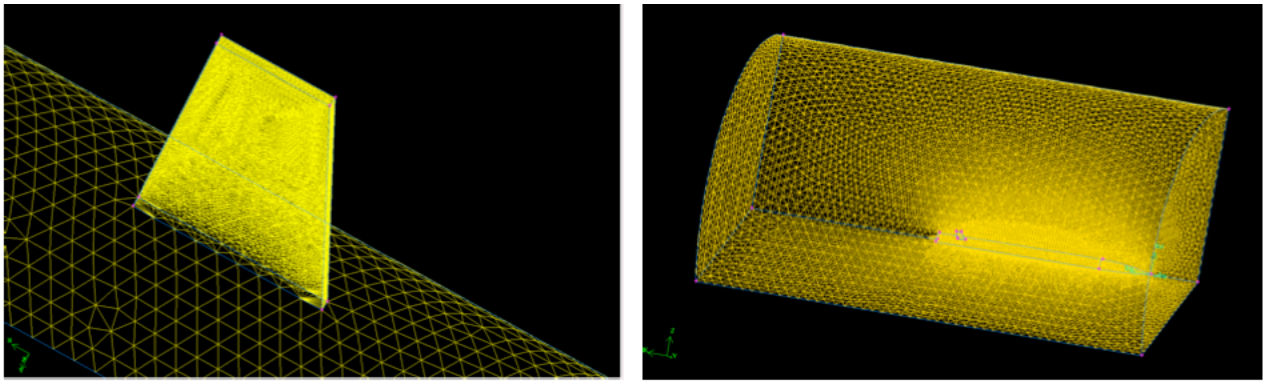

Figure 37. Computational Mesh for Javelin Fins and Body Tube.

To benchmark the highest overall drag value, highest velocity during flight, 185 m/sec (Mach 0.5) was chosen as the inlet condition. This peak velocity occurred at 640 meters above sea level. A laminar model and three different turbulence models were used to calculate the drag coefficient. The model was solved assuming and incompressible fluid using the SIMPLE scheme with first-order up-winding. In the interest of time, higher order solutions were not attempted. Table 7 summarizes the results. Not unexpectedly, the drag coefficient values presented in Table 7 are low when compared to the baseline calculations for the Javelin. Possible reasons for this difference include induced drag due to fin misalignment vehicle spin, local angle of attack variations during flight, and an improperly modeled vehicle base area. Taking these factors into account, the difference between the average incompressible turbulent drag coefficient of *0.2790* and the incompressible laminar drag coefficient (*0.2046*) is 0*.074*. This value comparable to the drag coefficient reduction observed in the flight data of *0.080*, and lends credence to the re-laminarization hypothesis. Ultimately, the reason for the dramatic decrease in drag from *flight 2* to the *flight 3* can only be discovered with significantly more experimentation and flight-testing. This is a luxury the Chimaera team did not have.

Table 7. Javelin Drag Coefficient for Various Viscosity/Turbulent Models.

Model	Drag Coefficient
Laminar	0.20464
Spalart-Allmaras	0.27690
k-epsilon	0.25172
k-omega	0.3084

4) Aerospike Ramp Pressures

Even though the C-BAS did not activate in-flight, pressure data were still successfully logged, and provided useful modeling information. This data can be used to infer the in-flight performance of the C-BAS had it actually operated. Figure 38 shows the differential pressure measurements collected from each pressure port. For each graph the profiles obtained from both port and starboard side ramps are plotted. Interestingly, as one moves aft on the ramp surface from port 1 to port 3, the surface pressures actually increases. This pressure rise indicates that a lowered subsonic surface velocity is produced by the free stream cross flow. As expected the maximum effect of the free stream flow occurs at the peak flight dynamics pressure. Figure 38d shows this comparison.

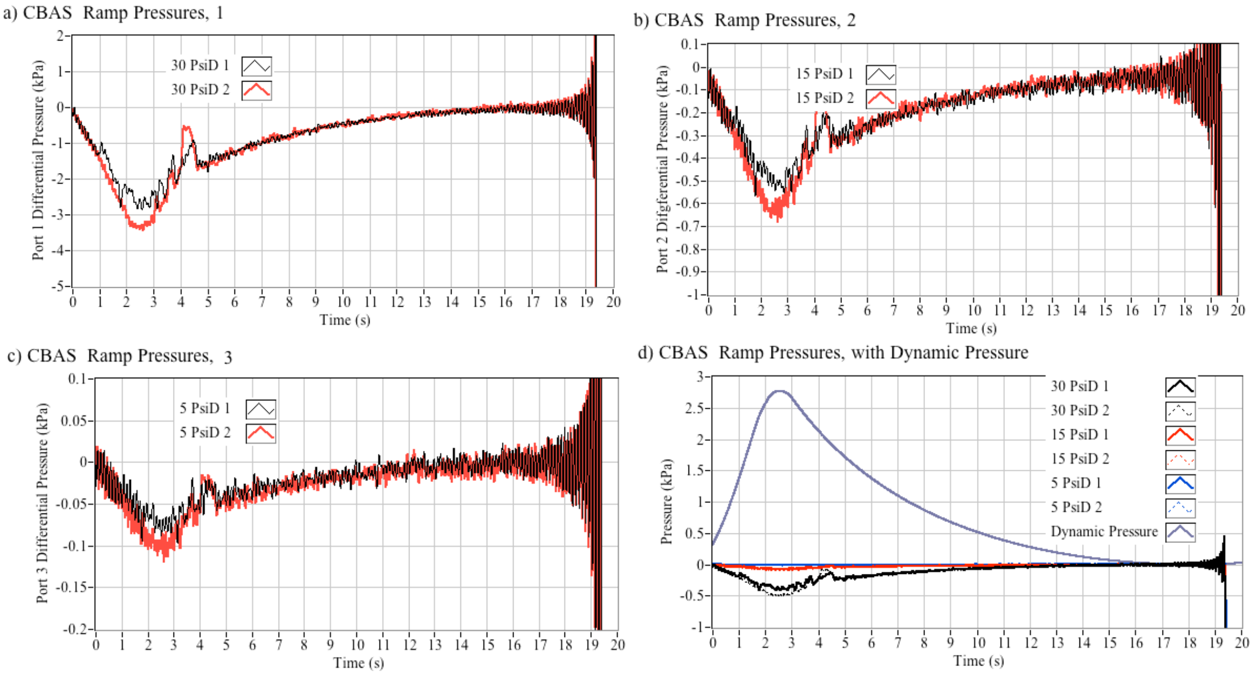

Figure 38. Aerospike Ramp In-Flight Pressure Time-of-Flight Profiles.

The differential pressure data of Figure 38 are normalized by dynamic pressure to calculate corresponding pressure coefficients. Figure 39 plots the recalculated pressure coefficients as a function of free stream Mach number. The interesting result is that the pressure coefficients on the ramps show very negligible effects due to Mach number – as least for the moderate subsonic pressures experienced in flight. Wang et al,[31] have observed that Mach number has a significant influence on cross-flow effects only under supersonic conditions -- so this result is not entirely unexpected.

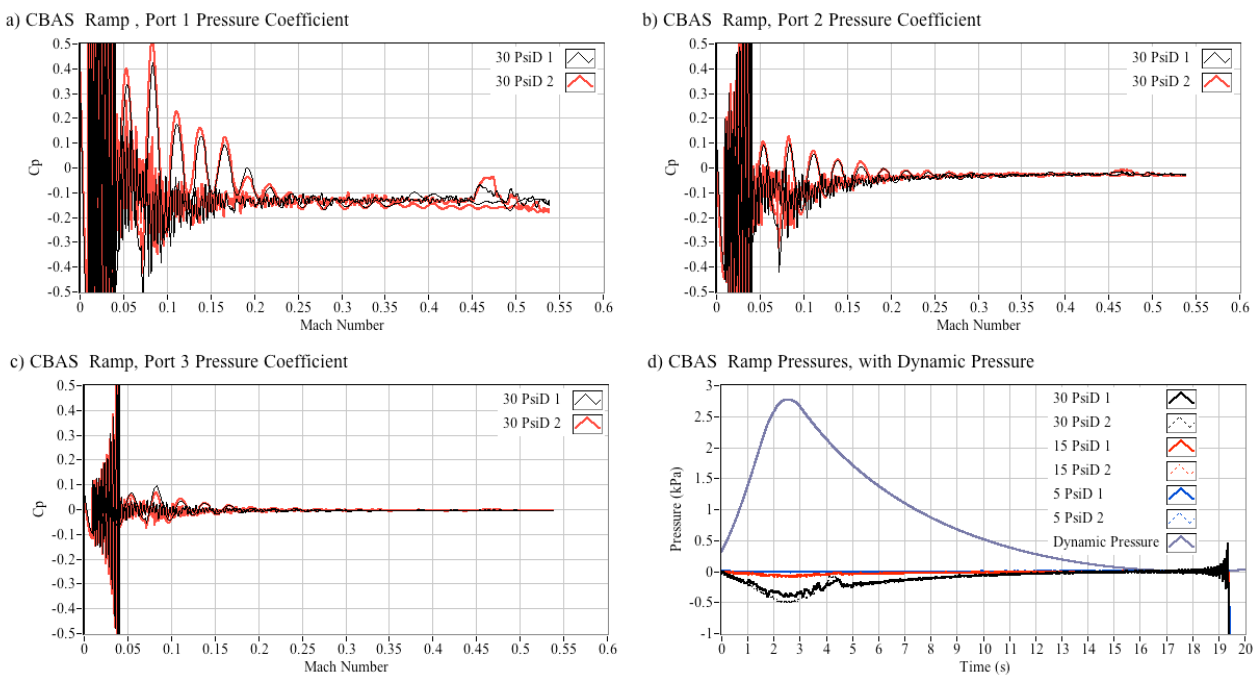

Figure 39. Aerospike Ramp In-Flight Pressure Coefficient Mach Number Profile.

When the mean pressure coefficients calculated from the C-BAS ground tests (Figure 29) are combined with the flight slipstream pressure coefficients, an in-flight linear subsonic performance model for the C-BAS thrusters is created. Figure 40 shows this result. Here the flight pressure coefficients, demonstrated to be independent of Mach number, are plotted as a function of the longitudinal distance down the spike ramp. The three pressure port coefficients have been curve fit to give a continuous distribution along the ramp surface. Similarly, the C-BAS ramp ground pressure coefficients, calculated as the surface ramp differential pressure divided by the plenum pressure

$$c_p = 10\left(\frac{P - p_\infty}{P_c}\right), \tag{34}$$

are plotted as function of the longitudinal distance down the ramp. These pressure coefficients are multiplied by a factor of 10 to give a similar display magnitude as the flight pressure coefficient data. The predicted in flight thrust levels can be calculated by integrating the pressure forces displaced on this figure along the length of the ramp, summing the two results, and adding the momentum thrust at the throat exit.

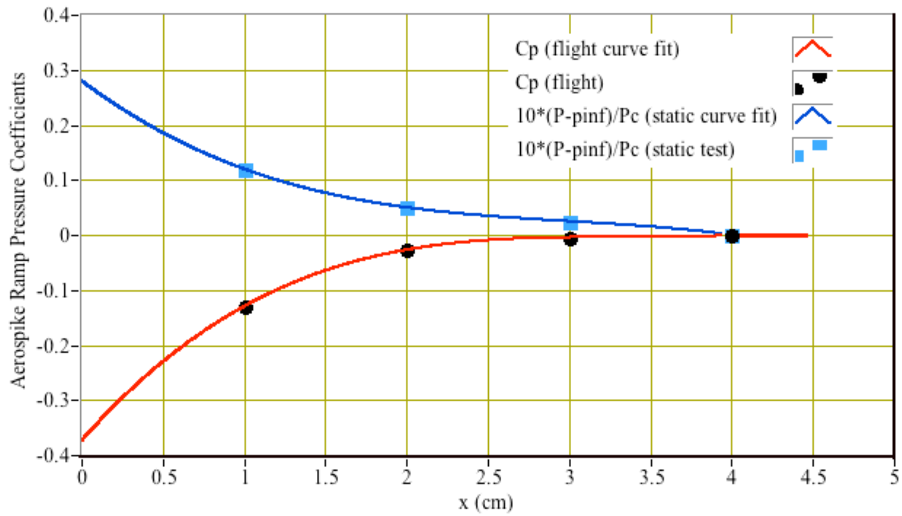

Figure 40. In-Flight Linear C-BAS Thruster Performance Model.

IX. Summary and Conclusion

This paper describes the outcome of a two-semester senior design course developed and implemented by the Mechanical and Aerospace Engineering Department at Utah State University. This design course was unique in that it specifically targeted the NASA University Student Launch Initiative (USLI) competition organized and directed by the Marshall Spaceflight Center in Huntsville AL. Targeting the USLI competition for the design automatically produces a clearly defined set of requirements that are inherently "less artificial" than project requirements that are arbitrarily assigned by the course instructor. The course materials adhere to the standards of the Accreditation Board for Engineering and Technology, and are constructed to be relevant to key research areas identified by NASA's Exploration Mission Directorate. This paper is offered as a case study of a successful capstone senior design class that achieved all of its educational and technical objectives. Ultimately the Utah State Chimaera design team was selected as the winner of the 2011 NASA launch competition. It is hoped that the materials presented in this paper will serve as a guide for other academic institutions wishing to under take a similarly ambitious project.

The design features a solid propellant primary rocket motor that provides a majority of launch impulse, and a secondary propulsion system that manages the energy level of the vehicle to reach a target apogee altitude. The secondary propulsion system was flown as the "engineering payload" for the USLI competition. The secondary system features a pulse-modulated cold gas bleed system with expansion ramps designed from aerospike nozzle theory. The energy management system was integrated with the airframe by placing the aerospike ramps around the primary solid motor case; this design added minimal aerodynamic drag to the configuration. Onboard navigation data are processed in a small onboard avionics computer to continuously estimate the total specific energy and potential altitude of the vehicle. When, required the onboard avionics activate the system to boost the energy level of the vehicle.

With all factors considered, The Javelin launch at the USLI competition was a success. With a flawless flight trajectory and parachute deployment, the only flight anomaly was an unexpected reduction of rocket drag when compared to the second qualification flight and pre-flight predictions. Because of the reduced drag, the energy bleed off during the ballistic phase of flight was lower than anticipated, and the overall energy level never crossed over the scheduled value for triggering C-BAS activation. Flight IMU data relayed wirelessly during flight clearly shows that the rocket had an otherwise nominal flight trajectory. While the C-BAS did not activate, in-flight pressure data was still successfully logged, and provided useful data. This data can be used to infer the in-flight performance of the C-BAS had it actually been operated.

From beginning to end, designing, reviewing, fabricating, and flying a high powered rocket that favorably represented of the College of Engineering at Utah State University provided an incredible learning experience not conventionally provided by academic coursework. Following the flight 1 crash, salvaging, rebuilding, and flight-testing a rocket of this complexity in a single week was a remarkable achievement for the Chimaera team. Recovering from this disaster to win the overall USLI competition title was real demonstration of student character. When the unthinkable happened and the rocket was lost to a crash, no finger pointing fingers and laying of blame occurred; instead the team as a whole responded like champions. Involvement in the accident investigation board, provided the team with the opportunity to learn from errors made, and will go a long way to making them better design engineers. As former Deputy Administrator of NASA Dr. Hugh Dryden has said, "[The purpose of flight research] is to separate the real from the imagined problems and to make known the overlooked and the unexpected."

Acknowledgements

The authors of this paper and the entire Chimaera student design team wish to thank the USU Dean of the College of Engineering, the USU Space Dynamics Lab, the Rocky Mountain Space Grant Consortium, and the Exploration Mission Directorate Education Office at Kennedy Space Center for funding this project. With out adequate funding this project could never have achieved the design complexity and success required to win the USLI competition. The team would also like to thank the Utah Section of the National Rocketry Association (UROC) and the Utah Section of the American Institute of Aeronautics and Astronautics (AIAA) for assisting students to achieve Tripoli Level I and II flight certifications and for providing technical oversight and peer review.

References

[1] *"National Association of Rocketry Safety Information,"* http://www.nar.org/safety.html, [Retrieved 7 July 2011].

[2] "National Fire Protection Association, Codes & Standards," http://www.nfpa.org/categoryList.asp?categoryID=124&URL=Codes%20&%20Standards, [Retrieved 7 July, 2011].

[3] *"Explosions, General Theory, Definitions,"* http://tracefireandsafety.com/VFRE-99/Theory/Definitions/definitions.htm, [Retrieved 7 July, 2011].

[4] "*NAR Certified Motors*," National Associate of Rocketry, http://www.nar.org/SanT/NARenglist.shtml, [Retrieved 4 December, 2010.]

[5] "Motor Performance Data Online," http://www.thrustcurve.org, [Retrieved 7 July 2011].

[6] *"Motor performance Data Online,"* http://www.thrustcurve.org/motorsearch.jsp?id=380, [Retrieved 7 July 2011].

[7] "Chimaera Advanced Student Built Rocketry, User documentation, http://Chimaera.usu.edu/projects/usli/documents, [Retrieved 7 July 2010].

[8] "Blue Tubes," http://www.apogeerockets.com/blue_tubes.asp, [Retrieved 11 July 2011].

[9] Lee, Ching-Che, and Thompson, D. D., "Fortran Program for Plug Nozzle Design,"NASA TM X-53019, Washington DC, July, 1964.

[10] Miyamoto, H., and Matsuo, A., and Kojuma, T., 42nd "Effects of Sidewall Configurations on Rectangular Plug Nozzle Performance," AIAA 2006-4373, AIAA Joint Propulsion Conference and Exhibit, sacramento, CA, 9-12 July, 2006.

[11] "R-DAS", AED electronics, http://www.aedelectronics.nl/rdas/links.htm, [retrieved 14 July 2011].

[12]"3DM-GX3-25, Miniature Attitude, Heading Reference SWystem (AHRS), MicroStrain Inc., http://www.microstrain.com/3dm-gx3-25.aspx, [Retrieved 8 June 2010].

[13] "PerfectFlite," http://www.perfectflite.com, [Retrieved 14 November 2010].

[14]"Gumstix, Dream, Design, Deliver," Gumstix, Inc., http://www.gumstix.com, [Retrieved 10 April 2010].

[15] "Bullet, Revolutionary Outdoor radio device," http://ubnt.com/bullet, [Retrieved 12 July 2011].

[16]"IEEE 802.11," Wikipedia, http://en.wikipedia.org/wiki/IEEE_802.11, [Retrieved 19 June 2011].

[17]"NI Labview," National Instruments, http://www.ni.com/labview, [Retrieved 8 June 2011].

[18] Etkin, B., *Dynamics of Atmospheric Flight*, John Wiley and Sons, New York, 1972, Chapt. 5.

[19] 3DM-GX3™-25, "Miniature Attitude heading Reference System, Technical Product Overview," MicroSAtrain, Inc. http://www.microstrain.com, pp. 2,3.

[20] "MiniAlt/WD™ User's Manual," PerfectFlite, Inc., www.perfectflite.com, pg, 22.

[21] Blake, William B., "Missile DATCOM User's Manual - 1997 Fortran 90 Revision", Air Force Research Laboratory, February 1998.

[22] "AeroCFD® 7.0, Model Rocket CFD Program for Microsoft Windows By AeroRocket," http://www.aerorocket.com/aerocfd.html, [retrieved 12 July, 2011].

[23] Drew, B, and Jen, A., "Pressure Drag Calculations on Axi-symmetric Bodies of Arbitrary Moldline", AIAA-90-0280,Reno, NV, 1990.

[24] Barrowman, J.S., "The Practical Calculation of the Aerodynamic Characteristics of Slender Finned Vehicles", Catholic University of America MS Thesis, March 1967.

[25] Whitmore, S. A., Naughton, J. W., and Sprague, S., "Wind-Tunnel Investigations of Blunt-Body Drag Reduction using Forebody Surface Roughness," AIAA-2001-0252, January 2001. *39th Aerospace Sciences Meeting and Exhibit, January 8-11, 2001, Reno, NV.*

[26] Kuethe, A., M., Chow, C., Y., *D*, 3rd ed, John Wiley & Sons, New York, 1976, pp. 258-262.

[27] "Cesaroni Pro 54®," http://www.pro38.com/products/pro54/motor.php, [Retrieved 14 July 2011].

[28] Dean, A. L., "Solid Edge V20"," MCAD Magazine, June 2006.

[29] "CFD Online," http://www.cfd-online.com/Wiki/Fluent_FAQ, [Retrieved 14 July 2011].

[30] "Flow Modeling Solutions for the Aerospace & Defense Industries," Fluent, Inc., http://www.fluent.com/solutions/aerospace/index.htm [Retrieved: 14 July 2007].

[31] Wang, C. H., Lui, Y., and Qin, L., Z., "Aerospike Nozzle Contour Design and Its Performance Validation," Acta Astronautica, Vol. 64, No. 11-12, June-July 2009, pp. 1264-1275.